

Magneto-Optical Tracking of Flexible Laparoscopic Ultrasound: Model-Based Online Detection and Correction of Magnetic Tracking Errors

Marco Feuerstein*, Tobias Reichl, Jakob Vogel, Joerg Traub, and Nassir Navab

Abstract—Electromagnetic tracking is currently one of the most promising means of localizing flexible endoscopic instruments such as flexible laparoscopic ultrasound transducers. However, electromagnetic tracking is also susceptible to interference from ferromagnetic material, which distorts the magnetic field and leads to tracking errors. This paper presents new methods for real-time online detection and reduction of dynamic electromagnetic tracking errors when localizing a flexible laparoscopic ultrasound transducer. We use a hybrid tracking setup to combine optical tracking of the transducer shaft and electromagnetic tracking of the flexible transducer tip. A novel approach of modeling the poses of the transducer tip in relation to the transducer shaft allows us to reliably detect and significantly reduce electromagnetic tracking errors. For detecting errors of more than 5 mm, we achieved a sensitivity and specificity of 91% and 93%, respectively. Initial 3-D rms error of 6.91 mm were reduced to 3.15 mm.

Index Terms—Electromagnetic tracking, hybrid tracking, image-guided surgery, laparoscopic surgery, optical tracking.

I. INTRODUCTION

ULTRASONOGRAPHY is an appealing technology to physicians because of its noninvasiveness, wide availability, flexible handling, and low cost. Having been used primarily for diagnosis in the past, intraoperative and laparoscopic ultrasonography today play a greater role in abdominal surgery. The liver, biliary tract, and pancreas are the main application areas of intraoperative and laparoscopic ultrasound, for instance to detect liver lesions such as metastases. Unfortunately, the success of laparoscopic ultrasonography is operator dependent; for novice surgeons in particular it is often difficult or even impossible to detect target objects such as common bile duct stones intraoperatively [1]. The major reasons given for this are the missing tactile feedback, the difficulty of interpreting laparoscopic ultrasound images, a limited degree of positioning through the trocar access, disorientation caused by

the constantly changing imaging plane, and a lack of awareness of the transducer tip location (the tip needs to be constantly observed in the laparoscopic camera images in order to avoid inadvertent injury) [1]–[3].

Several groups have tried to address some of these issues by providing navigated laparoscopic ultrasound: the position and orientation (“pose”) of the ultrasound transducer is estimated so that its shape and *B*-scan images can be visualized in relation to the patient, other surgical instruments, or preoperative and intraoperative imaging data. This can provide great support to surgeons using laparoscopic ultrasound in cancer staging, radio frequency ablation, and other diagnostic and therapeutic procedures.

To estimate the pose of a transducer with a rigid tip, a robot or an optical tracker (OT) may be used [4]. In the latter case, a rigid optical marker can be attached to the transducer handle to assure its continuous visibility. Several groups have also tried to localize rigid laparoscopic instruments in laparoscopic images by using advanced image processing techniques [5]–[9]. However, the laparoscopic transducers most commonly used and preferred by surgeons have a flexible tip that can be steered left, right, up or down. The tip can also be bent by external pressure from organ surfaces. Due to the missing line of sight to the flexible transducer tip, an OT cannot be used exclusively to localize this tip. A robot could only be used if the flexible ultrasound probe is fully integrated into the end-effector. To the authors’ knowledge no such system exists. Promising alternatives are the use of an electromagnetic tracker (EMT) localizing a sensor attached to the tip [10]–[12] or fully incorporated into the tip [13], or a magneto-optical tracker, i.e., the combination of an OT and an EMT [14]–[16].

When using an EMT clinically, a significant problem is the distortion of the magnetic field, which leads to tracking errors. This distortion can be caused by metallic or electrically powered objects inside or close to the working volume, for instance surgical instruments, an operating table, or imaging devices such as a C-arm or a computed tomography scanner. Depending on the operating room setup and instrumentation, tracking errors of several millimeters or even centimeters can occur [17], [18]. To compensate for erroneous measurements caused by stationary objects, various calibration techniques have been proposed [19]. They usually require the user to acquire a set of well distributed (distorted) measurements within the tracking volume and corresponding (undistorted) reference measurements to compute a field distortion function that is based on lookup tables or polynomials. Unfortunately, this function can only compensate for

Manuscript received June 09, 2008; revised October 13, 2008. First published February 10, 2009; current version published May 28, 2009. Asterisk indicates corresponding author.

*M. Feuerstein is with the Department of Media Science, Graduate School of Information Science, Nagoya University, Nagoya 464-8603, Japan (e-mail: fmarco@suenaga.m.is.nagoya-u.ac.jp).

T. Reichl, J. Vogel, J. Traub, and N. Navab are with the Chair for Computer Aided Medical Procedures and Augmented Reality, Technische Universität München, 85748 Garching, Germany (e-mail: reichl@cs.tum.edu; vogelj@cs.tum.edu; traub@cs.tum.edu; navab@cs.tum.edu).

Color versions of one of more of the figures in this paper are available online at <http://ieeexplore.ieee.org>.

Digital Object Identifier 10.1109/TMI.2008.2008954

stationary distortion field errors, so that the calibration process has to be repeated for every new operating room setup before an intervention. In the best case, calibration could be performed intraoperatively only for the region of interest using a special distortion measurement apparatus that fits to a trocar, as proposed by the authors of [16] for laparoscopic 3-D ultrasound.

However, dynamic changes of the field distortion, caused for example by the intraoperative relocation of the magnetic field generator or movement of instruments, cannot be compensated for by the previously computed distortion functions. A first step towards the intraoperative detection of erroneous measurements caused by metallic objects distorting the field was presented by [20] and later by [21]. They incorporate two magnetic sensors into a pointer so that redundant measurements can be obtained. Measured deviations of the fixed distance between the two sensors are used as a plausibility value.

Our paper introduces two new methods to detect and reduce dynamic electromagnetic tracking errors online, i.e., intraoperatively without a precomputed distortion function. This is achieved by a *hybrid magneto-optical tracking setup*. The laparoscopic ultrasound transducer is tracked electromagnetically as well as optically, and the EMT is itself tracked optically. After *magneto-optical coregistration*, i.e., alignment of the EMT and OT coordinate frames, we can get redundant tracking data, where the OT provides undistorted, more reliable measurements than the EMT. We employ this redundancy in our first, *tracking redundancy-based approach*: comparing measurements of an optical marker and a magnetic sensor, both rigidly attached to the transducer shaft, we are able to detect deviations between the two measurements. These deviations can be used to predict tracking errors of another magnetic sensor mounted on the flexible transducer tip. In a second, more sophisticated *model-based approach*, we model all possible tip movements relative to the optically tracked shaft using only two rotation angles and thus reduce the degrees-of-freedom (DOF) of any tip movement from six to two. By discarding the four redundant DOF, each distorted measurement of the magnetic sensor on the transducer tip can be mapped onto the model for error correction.

For our two online error detection and correction approaches, we evaluate not only 3-D errors, but also 2-D overlay errors during camera superimposition, which is useful e.g., for medical augmented reality [22], where the in-plane error is most important. Therefore, we also incorporate and calibrate a laparoscope camera that is localized by the OT. For the sake of completeness, we also briefly describe our ultrasound calibration techniques to determine the location of the ultrasound plane in OT coordinates, which is important for the final application [23], [24]. We also compare our results on error detection and correction to the findings of other groups [20], [21].

II. SYSTEM SETUP

The hardware setup we used for all calibration and evaluation steps consists of the following components (see Fig. 1): a flexible laparoscopic linear array transducer (LAP8-4, 5 MHz, 10 mm diameter) connected to a SONOLINE Omnia ultrasound system from Siemens Medical Solutions (Mountain

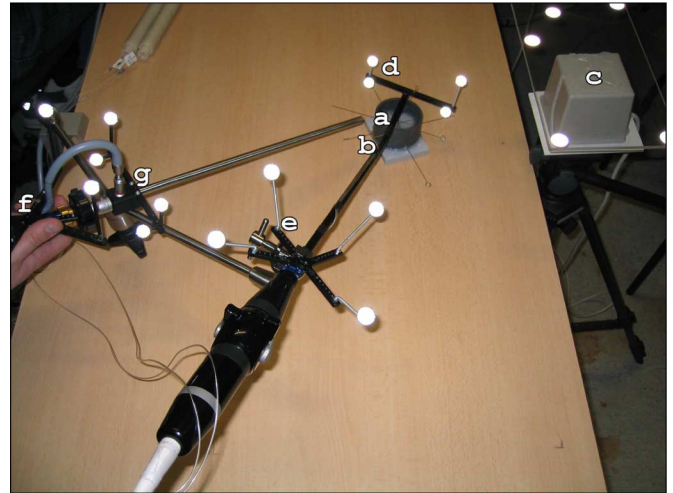


Fig. 1. System setup used for calibration and evaluation. Two magnetic sensors are attached to the laparoscopic ultrasound transducer, one to its flexible tip (a) and one to the rigid shaft (b); see Fig. 2 for a close-up of (a) and (b). The magnetic field generator representing our electromagnetic tracker (c) is itself tracked by an optical tracking system. The optical tracking system also localizes two optical markers attached to the ultrasound transducer, one (temporarily) to its flexible tip (d) and another to its rigid shaft (e). In addition, the laparoscope (f) and its telescope (g) are tracked optically.

View, CA), a laparoscopic camera with a forward-oblique 30° HOPKINS telescope from KARL STORZ GmbH & Co. KG (Tuttlingen, Germany), a standard workstation PC including two analog frame grabbers (for capturing the transducer and camera video in real time), and a hybrid magneto-optical tracking setup. The OT consists of 4 ARTrack2 cameras and a book-size PC running the DTrack tracking software, both provided by Advanced Realtime Tracking GmbH (Weilheim, Germany). The EMT in use is a 3-D Guidance unit from Ascension Technology Corporation (Burlington, VT) equipped with a midrange transmitter for magnetic field generation and 1.3 mm sensors in vinyl, which have a total diameter of 1.7 mm including the vinyl tubing. Time synchronization of all input data streams and visualization is performed by our medical augmented reality software platform CAMPAR [25].

We denote a rigid arrangement of at least three noncollinear and nonsymmetric retro-reflective spheres, which are localized by the OT, as an optical marker. Magnetic sensing coils localized by the EMT are denoted as magnetic sensors. To localize all instruments, several optical markers and magnetic sensors are used. In addition to an optical marker, which is attached to the transducer shaft (below referred to as OM_{shaft}), two magnetic sensors are attached to the transducer: one to the flexible tip (MS_{tip}), and the other to the rigid shaft (MS_{shaft}), at a distance of about seven centimeters (see Fig. 2). Another optical marker is mounted on the EMT (OM_{EMT}). This setup allows us to co-register the EMT and the OT and to obtain redundant tracking information for the rigid transducer shaft (see Sections III-A3 and III-B). Finally, two optical markers are attached to the laparoscopic camera, one to the head (OM_{lap}) and another to the telescope shaft (OM_{scope}), to adjust for telescope rotations (see Section III-A1).



Fig. 2. Close-up of the proximal part of the ultrasound transducer with a magnetic sensor attached to the transducer tip (a) and one attached to the transducer shaft (b).

III. METHODS

In the following section, we describe all required system calibration steps in order to detect and correct magnetic tracking errors when the flexible tip of the laparoscopic ultrasound transducer is in the close vicinity of ferromagnetic and/or electrically conductive material.

A. Offline System Calibration

The main purpose of all system calibration steps is to bring the local coordinate frame associated with each instrument, optical marker, or magnetic sensor into the same world coordinate system, chosen here to be the OT coordinate frame (see Fig. 3). Furthermore, all tracking and video data streams need to be tagged with time stamps and synchronized; see our previous work incorporating temporal calibration [23], [24] for further details. Finally, our new error estimation methods require an exact modeling of the transducer axis as well as possible transducer tip movements. This is described in Sections III-A4 and III-A5.

1) *Laparoscope Camera Calibration:* During laparoscope calibration, the camera projection geometry including distortion coefficients and the transformation ${}^{OM_{lap}}T_C$ from the camera frame to the coordinate frame of the optical marker on the laparoscope (via the coordinate frame of the optical marker on the telescope) are estimated. This can be done by using standard camera and hand-eye calibration techniques based on a planar checkerboard pattern and is described in more detail in various publications, for instance in our prior work [26]. For hand-eye calibration, see Section III-A3. It is important to note that the rotational offset, which is introduced when rotating the oblique telescope shaft around its longitudinal axis against the camera head, needs to be corrected for. An elegant solution to this problem was proposed by [27]. Instead of attaching a rotary encoder to the camera head to determine the current rotation angle of the telescope, we use the OT to estimate the relative rotation between the optical markers on the telescope and laparoscope, similar to [28].

2) *Laparoscopic Ultrasound Calibration:* For the determination of the pixel scaling of the ultrasound *B*-scan plane and the transformation ${}^{MS_{tip}}T_{US}$ between the plane and the coordinate frame of the magnetic sensor on the transducer tip, a single-wall calibration as proposed by the Cambridge group is performed [29]–[31]. We acquire ultrasound images of a nylon membrane stretched over a planar frame and immersed in a water bath [32], so that the nylon membrane is imaged as a fairly straight line that can be automatically segmented in the *B*-scan images. Several poses of the magnetic sensor as well as corresponding *B*-scan

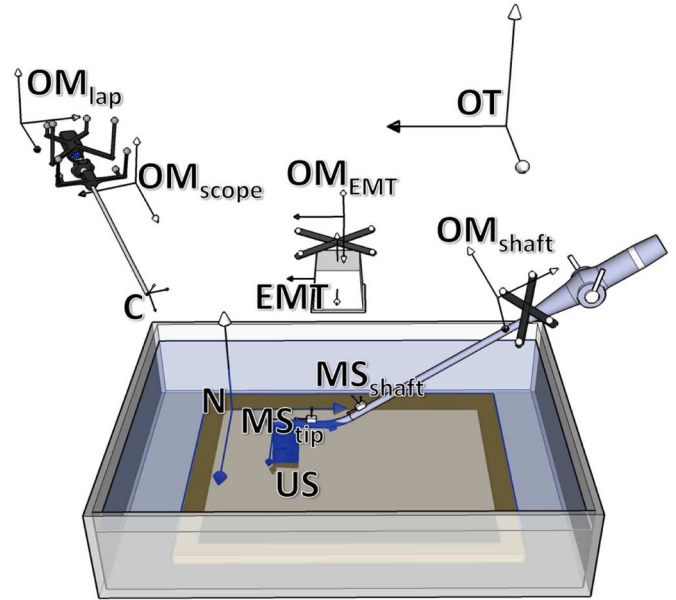


Fig. 3. All coordinate frames shown need to be brought into a common world coordinate system during system calibration. The optical tracker defines our world coordinate frame (OT). During laparoscope camera calibration, we determine the relation between the coordinate frames of the optical marker on the laparoscope (OM_{lap}), the optical marker on the telescope (OM_{scope}), and the camera (C). The origin of C coincides with the camera center of our pinhole camera model. During ultrasound calibration, we compute the rigid transformation between the coordinate frame of the ultrasound *B*-scan plane (US) and the magnetic sensor on the tip (MS_{tip}) by means of a temporarily used nylon membrane (N). During magneto-optical coregistration, we estimate the rigid transformations between the coordinate frame of the EMT and the optical marker attached to it (OM_{EMT}) as well as between the coordinate frames of the magnetic sensor (MS_{shaft}) and the optical marker (OM_{shaft}) on the shaft. The temporary optical marker, which is attached to the transducer tip and used for evaluation, and its coordinate frame (OM_{tip}) are not shown here.

images of the membrane inside a water bath are then acquired, following the calibration protocol of the Cambridge group to ensure numeric stability for all six DOF of ${}^{MS_{tip}}T_{US}$.

3) *Magneto-Optical Coregistration:* The process of aligning two tracking coordinate frames is referred to as coregistration or tracker alignment [33]. Similar to the authors in [34], we use a hybrid tracking approach by combining magnetic and optical tracking. The EMT is itself tracked using the OT so that any data acquired by the EMT can be transformed into the OT coordinate frame.

During magneto-optical coregistration we determine the transformation ${}^{OT}T_{EMT} = {}^{OT}T_{OM_{EMT}} {}^{OM_{EMT}}T_{EMT}$. As the optical marker attached to EMT is continuously localized by the OT, we obtain ${}^{OT}T_{OM_{EMT}}$ in real time and only need to determine the static transformation ${}^{OM_{EMT}}T_{EMT}$ from the coordinates of the EMT to the coordinates of the optical marker attached to it. Additionally, for the tracking redundancy-based error detection and correction methods described in Section III-B, the fixed Euclidean transformation ${}^{OM_{shaft}}T_{MS_{shaft}}$ between the coordinate frames of the magnetic sensor and the optical marker attached to the shaft needs to be estimated.

To compute ${}^{OM_{shaft}}T_{MS_{shaft}}$, the transducer is moved to $n \geq 3$ positions with distinct rotation axes. At each position $i = 1 \dots n$, we acquire measurements of the poses ${}^{OT}T_{OM_{shaft}(i)}$ of

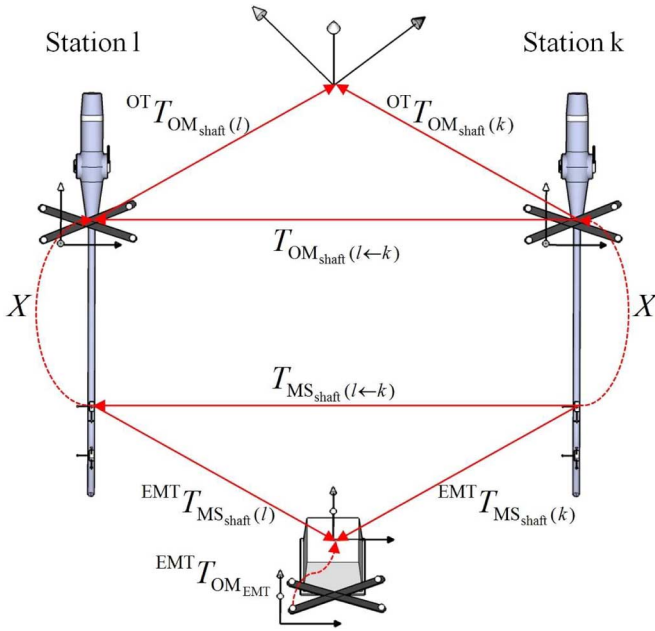


Fig. 4. During magneto-optical coregistration, we compute the unknown transformations X and ${}^{\text{EMT}}T_{\text{OM_EMT}}$, visualized here by dashed lines. From at least three transducer positions with distinct rotation axes (two positions k and l are shown here), we compute all possible unidirectional motion pairs between these positions, e.g., between positions k and l the pair $T_{\text{OM_shaft}(l \leftarrow k)}$ representing the motion of the optical marker and $T_{\text{MS_shaft}(l \leftarrow k)}$ representing the motion of the magnetic sensor. From these motion pairs, we can generate an overdetermined system of linear equations to solve for both desired transformations.

the optical marker and ${}^{\text{EMT}}T_{\text{MS_shaft}(i)}$ of the magnetic sensor (both attached to the transducer shaft) in the optical coordinate frame and in the electromagnetic coordinate frame, respectively (see Fig. 4 for two exemplary positions k and l).

All $m = n(n-1)/2$ possible unidirectional motion pairs between these positions can now be computed, e.g., between positions k and l the pair $T_{\text{OM_shaft}(l \leftarrow k)} = ({}^{\text{OT}}T_{\text{OM_shaft}(l)})^{-1} \cdot {}^{\text{OT}}T_{\text{OM_shaft}(k)}$ representing the motion of the optical marker and $T_{\text{MS_shaft}(l \leftarrow k)} = ({}^{\text{EMT}}T_{\text{MS_shaft}(l)})^{-1} \cdot {}^{\text{EMT}}T_{\text{MS_shaft}(k)}$ representing the motion of the magnetic sensor. For all motion pairs between positions k and l , the relation $T_{\text{OM_shaft}(l \leftarrow k)} \cdot X = X \cdot T_{\text{MS_shaft}(l \leftarrow k)}$ with $X = {}^{\text{OM_shaft}}T_{\text{MS_shaft}}$ holds.

All motions of the optical marker are now stacked to a matrix $A_{4m \times 4}$ and all corresponding motions of the magnetic sensor are stacked to a matrix $B_{4m \times 4}$, so both A and B contain m homogeneous transformation matrices. They are related to each other by the equation system $AX = XB$.

This equation system actually originated from robotics, where the rigid transformation X between a camera (“eye”) and a robot arm (“hand”) holding the camera was estimated using “hand–eye calibration” [35], [36]. We use a dual quaternions approach [37] to solve for X .

The same n transducer positions are also used to estimate the rigid transformation ${}^{\text{EMT}}T_{\text{OM_EMT}} = ({}^{\text{OM_EMT}}T_{\text{EMT}})^{-1}$ between the coordinate frame of the optical marker attached to the EMT and the EMT coordinate system, but this time generating motion pairs with assuming the ultrasound transducer to be stationary and the EMT and OT coordinate frames to perform the

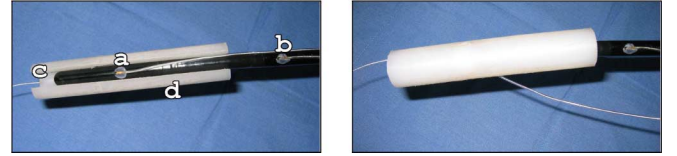


Fig. 5. Transducer axis calibration. The transducer axis is calibrated both in relation to the local coordinate system of the magnetic sensor attached to the tip (a) and, in a second step not shown here, in relation to the coordinate system of the magnetic sensor on the shaft (b). To do this, a plastic cylinder (d) is put over the transducer tip with an additionally attached sensor (c) on the left end. The plastic cylinder is rotated at least 360° , flipped, and rotated another 360° or more.

motions. Further details can be found in our previous work [38], including a derivation of the exact transformations used.

In a final optimization step, the two coregistration matrices ${}^{\text{OM_shaft}}T_{\text{MS_shaft}}$ and ${}^{\text{EMT}}T_{\text{OM_EMT}}$ are optimized for all recorded positions by the Levenberg–Marquardt algorithm [39]. The 4×4 matrix $T_\delta = \begin{bmatrix} R_\delta & t_\delta \\ 0 & 1 \end{bmatrix}$ resulting from the transformation chain starting at “magnetic sensor (MS_shaft) to optical marker (OM_shaft) to OT to optical marker (OM_EMT) to EMT to magnetic sensor (MS_shaft),” which theoretically is an identity matrix, represents the accumulated transformation errors

$$T_\delta = {}^{\text{MS_shaft}}T_{\text{EMT}} {}^{\text{EMT}}T_{\text{OM_EMT}} {}^{\text{OM_EMT}}T_{\text{OT}} \times {}^{\text{OT}}T_{\text{OM_shaft}} {}^{\text{OM_shaft}}T_{\text{MS_shaft}}. \quad (1)$$

For the Levenberg–Marquardt optimizer, we chose a cost function δ that weights translation to rotation errors 1:3:

$$\begin{aligned} \delta &= \delta_{\text{trans}} + 3 \cdot \delta_{\text{rot}} \\ &= \|t_\delta\| + 3 \cdot \frac{180}{\pi} \cdot \arccos\left(\frac{\text{trace}(R_\delta) - 1}{2}\right) \end{aligned} \quad (2)$$

where the translation error δ_{trans} is the norm of t_δ and the rotation error δ_{rot} is the rotation angle of R_δ , decomposed into axis-angle parameters. This 1:3 ratio reflects the root mean square (rms) error ratio provided independently by the two tracking system manufacturers: The rms measurement errors of the OT are stated as 0.4 mm (position) and 0.12° (orientation), the static rms errors of the EMT as 1.4 mm and 0.5° . Specifications of the typical accuracy of both tracking systems are available from AR Tracking¹ and Ascension Technology², respectively.

4) *Transducer Axis Calibration*: For modeling the transducer tip movements (see next Section III-A5), the transducer axis is first estimated in relation to the magnetic sensors attached to the shaft and to the tip. This can be done by putting a plastic cylinder, which contains an additional magnetic sensor on one end (see Fig. 5), over the transducer shaft. For each of the rigid part and the flexible part of the transducer shaft, the plastic

¹<http://www.ar-tracking.de>

²<http://www.ascension-tech.com>



Fig. 6. Typical bending region usually found in endoscopic instruments. Four Bowden cables are pairwise and alternately connected to every second link of the bending region. They are often controlled by steering levers, where each pair of cables is connected to the same lever.

cylinder is rotated at least 360° , flipped, and rotated another 360° or more. During each rotation, the measurements of the additional magnetic sensor are transformed into the local coordinate frames of the magnetic sensor on the shaft and tip, respectively. Each acquired point cloud $X_i, i = 1 \dots m$ is then fitted to a cylinder with radius r around the transducer axis, which is defined by the 3-D point \mathbf{b} on the axis closest to the magnetic sensor on the shaft (or on the tip, for the other point cloud) and a 3-D unit vector \mathbf{d} pointing along the axis to the tip of the transducer. The following function is minimized by the Levenberg–Marquardt optimizer:

$$\sum_{i=1}^m |r - \|\mathbf{d} \times (\mathbf{b} - X_i)\||. \quad (3)$$

Finally, two transducer axes are defined, one in coordinates of the magnetic sensor on the tip by the base point $\mathbf{b}_{\text{MS}_{\text{tip}}}$ and the unit directional vector $\mathbf{d}_{\text{MS}_{\text{tip}}}$, and the other in coordinates of the sensor on the shaft by $\mathbf{b}_{\text{MS}_{\text{shaft}}}$ and $\mathbf{d}_{\text{MS}_{\text{shaft}}}$.

5) *Transducer Tip Modeling*: Modeling the transducer tip serves two purposes. First, the model can provide all 3-D information necessary to overlay a virtual model of the ultrasound transducer onto the measured location, which can be useful for the development of a navigation system. Second, and more importantly, if built relative to the optical marker on the transducer shaft, it can be used to detect and partially correct tracking inaccuracies (see Section III-B2).

The ultrasound transducer contains not a single joint, but an elongated bending region with several links extending over approximately 3 cm, similar to the one shown in Fig. 6.

Since the horizontal and vertical bending of the tip is controlled by two steering levers and each lever offers seven positions, 49 tip poses are manually selectable. The tip can also be bent by external pressure, allowing us to model continuous motions on a curved surface to approximate all possible tip poses.

The motions of the bending region on this surface can be approximated using an “extended cardioid of revolution.” A cardioid is usually constructed in 2-D by revolving a circle around another one with the same radius r . This corresponds to an identical angular motion of two links of length r and $2r$, and the construction can be extended to a greater number of links (see Fig. 7 for six links). Spatial motions about two orthogonal rotation axes define a 3-D surface. This surface can be constructed by rotating the extended cardioid around its central axis, resulting in a surface of revolution. If we look at the position of the transducer tip rather than the last link, we have to introduce another outward translation, so the actual geometric shape of the attainable tip poses is similar to, but not exactly the same as, our extended cardioid of revolution.

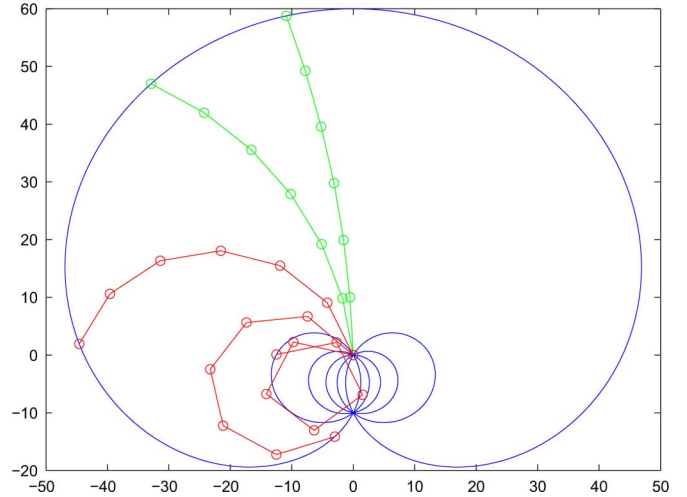


Fig. 7. Cross-section of the extended cardioid of revolution, describing all possible rotations of the bending region about one axis. The bending links are shown for several angles (green: $3^\circ, 10^\circ$; red: $25^\circ, 48^\circ, 77^\circ$), not all of which are actually attainable due to physical constraints (green ones are attainable, red ones are only theoretically possible).

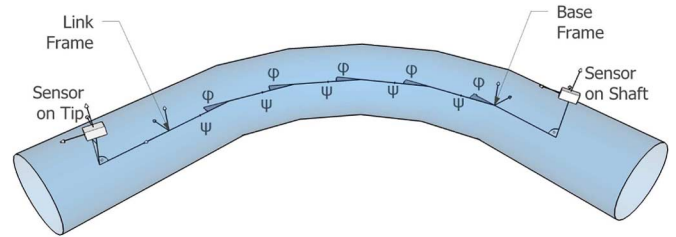


Fig. 8. Mathematical model of the tip of the flexible ultrasound transducer—only the rotation ϕ about the x axis is visualized here, the rotation ψ about the y axis is zero.

The extended cardioid of revolution only models the bending region of the transducer. To change from the coordinate frame of the magnetic sensor on the tip into that of the sensor on the shaft, a chain of transformations is modeled, as shown in Fig. 8.

Transformation Chain: First, the coordinate frame of the magnetic sensor on the tip is rotated and translated into the “link frame” in such a way that the z axis points along the transducer axis. This transformation ${}^{\text{Link}}T_{\text{MS}_{\text{tip}}}$ has six DOF, i.e., three rotations and one translation along the x axis of the sensor to align the sensor with the transducer axis, followed by a rotation about and a translation along the transducer axis.

Starting at the link frame, n short links follow, which approximate the possible tip movements. In an alternating manner, each link rotates the transducer axis by ψ about the y axis or by ϕ about the x axis, respectively. No rotation about the z axis is assumed. Each link introduces a translational offset t_z along the z axis. Including n , the number of links, ${}^{\text{Base}}T_{\text{Link}}$ in total has four DOF

$${}^{\text{Base}}T_{\text{Link}} = \underbrace{T_{\text{Link}}(\phi)}_1 \cdot \underbrace{T_{\text{Link}}(\psi)}_2 \cdot \underbrace{T_{\text{Link}}(\phi)}_3 \cdot \dots \quad (4)$$

n times

where

$$\mathbf{T}_{\text{Link}}(\phi) = \begin{pmatrix} 1 & 0 & 0 & 0 \\ 0 & \cos(\phi) & -\sin(\phi) & 0 \\ 0 & \sin(\phi) & \cos(\phi) & t_z \\ 0 & 0 & 0 & 1 \end{pmatrix}$$

$$\mathbf{T}_{\text{Link}}(\psi) = \begin{pmatrix} \cos(\psi) & 0 & \sin(\psi) & 0 \\ 0 & 1 & 0 & 0 \\ -\sin(\psi) & 0 & \cos(\psi) & t_z \\ 0 & 0 & 0 & 1 \end{pmatrix}.$$

This behavior of alternating links is inspired by the real nature of the bending region, where four Bowden cables controlled by the steering levers are pairwise and alternately connected to every second link (see Fig. 6).

After the bending region, i.e., at the base frame, a final translational and rotational offset ${}^{\text{MS}_{\text{shaft}}}\mathbf{T}_{\text{Base}}$ is applied to align the final tip coordinate frame with the magnetic sensor on the shaft, which has five DOF. Actually, ${}^{\text{Link}}\mathbf{T}_{\text{MS}_{\text{tip}}}$ and ${}^{\text{MS}_{\text{shaft}}}\mathbf{T}_{\text{Base}}$ would both have six DOF. However, one DOF of the rotation about the transducer (z) axis is not needed for ${}^{\text{MS}_{\text{shaft}}}\mathbf{T}_{\text{Base}}$, as it can be entirely compensated for by just altering the combination and magnitudes of ϕ and ψ . Conversely, one more DOF is needed for the rotation about the transducer axis included in ${}^{\text{Link}}\mathbf{T}_{\text{MS}_{\text{tip}}}$ to adjust for the fact that the sensors can be mounted at different angles about the transducer axis, i.e., assuming ϕ and ψ to be 0, the line through the origins of the two sensor coordinate frames will not be parallel to the transducer axis.

The final model transformation, from coordinates of the magnetic sensor on the transducer tip, into coordinates of the sensor on the transducer shaft, can be described by

$${}^{\text{MS}_{\text{shaft}}}\mathbf{T}_{\text{MS}_{\text{tip}}} = {}^{\text{MS}_{\text{shaft}}}\mathbf{T}_{\text{Base}} \cdot {}^{\text{Base}}\mathbf{T}_{\text{Link}} \cdot {}^{\text{Link}}\mathbf{T}_{\text{MS}_{\text{tip}}}. \quad (5)$$

For error estimation (see Section III-B2), the model is actually not built relative to the magnetic sensor on the transducer shaft, but relative to the optical marker. Therefore, during modeling, only the additional static transformation ${}^{\text{OM}_{\text{shaft}}}\mathbf{T}_{\text{MS}_{\text{shaft}}}$ needs to be applied to magnetic sensor coordinates to determine optical marker coordinates.

Parameter Optimization: All parameters except angles ϕ and ψ remain constant for a given configuration and can be computed offline. Given that the transducer axes in relation to the sensors on the shaft and tip have been calibrated, only five model parameters have to be estimated offline. These are the translation along the rigid shaft axis (contained in ${}^{\text{MS}_{\text{shaft}}}\mathbf{T}_{\text{Base}}$), the length of the bending region ($n \cdot t_z$), the number of links in the bending region (which can be initialized or fixed to $n = 12$, because many surgical instruments have 12 links like the one in Fig. 6), the angle of rotation about the tip axis, and the length of translation along the tip axis (both contained in ${}^{\text{Link}}\mathbf{T}_{\text{MS}_{\text{tip}}}$).

For every selectable position of the two control levers, the pose of the magnetic sensor on the tip in relation to the one on the shaft is recorded in a distortion-free environment, i.e., without ferromagnetic or electrically powered materials in the close vicinity. Then the remaining model parameters are optimized numerically using the Levenberg–Marquardt algorithm. The model has to be computed only once, when the magnetic sensors are attached to the transducer.

At runtime, i.e., intraoperatively, the remaining two DOF of the rotations ϕ and ψ about the x and y axis can be numerically optimized by the Levenberg–Marquardt optimizer. Either the translation to the magnetic sensor on the tip, rotation difference, or a combination of both can be minimized. In our experiments we used a 1:3 weighting of translation in millimeters to rotation in degrees, as in the magneto-optical coregistration [see (2)].

Applicability of the Model: We constructed the model of the transducer tip according to our observations and studies of the behavior of the Bowden cables pulling the bending region. However, our model is only an approximation inspired by the general design of flexible endoscopic instruments. Of course, other endoscopic instruments can also have different mechanical tip designs, so it may not be sufficient to apply our model to them without further testing and/or modification.

As seen in our evaluation of the transducer tip model (see Section IV-D and Fig. 9), the transducer tip mostly follows the model, independently of the order of selection of the two steering levers. The model is less precise when the tip is bent more than halfway between its neutral position and maximally bent position (“neutral position” corresponds to ϕ and ψ being approximately zero). We suspect the reasons for this to be the nonideal elasticity of the bending region and its exposure to large mechanical forces that are irregularly distributed over the links. However, our clinical partner reported that intraoperatively the transducer tip is seldom bent more than halfway, i.e., the transducer tip is rarely bent to the leftmost or rightmost preset deflection setting, or beyond a single of the preset deflections up and down. In all, three preset deflections are possible in each of the four directions (up/down/left/right), in addition to the neutral position.

B. Tracking Error Detection and Correction

We propose approaches for the detection and correction of dynamic sources of electromagnetic tracking errors which can be divided into redundancy-based, model-based, and vision-based tracking, where the latter is described in more detail in our previous work [24].

1) *Tracking Redundancy-Based Approach:* Each approach to correcting static erroneous measurements that is based on hybrid (and thus redundant) tracking of an object (e.g., [40] or [41], that use magneto-optical tracking), can also be used for error detection. Such an approach is however not intended to detect and correct *dynamic* sources of errors, as it is performed only once to create a static distortion function of the magnetic field. Furthermore, magneto-optical tracking cannot be applied to the tip of the ultrasound transducer due to its flexibility and the lack of line of sight to the optical cameras.

Therefore, one idea for an error detection method is to estimate errors at the magnetic sensor on the shaft instead and, for a simple error correction, transfer them to the magnetic sensor on the tip.

a) *Error Detection:* Similar to the authors of [20] and [21], who connect two magnetic sensors rigidly to each other and use the deviation of their distance to detect field distortions, our simple error detection method is based on tracking redundancy. However, we do not use two magnetic sensors, but one optical

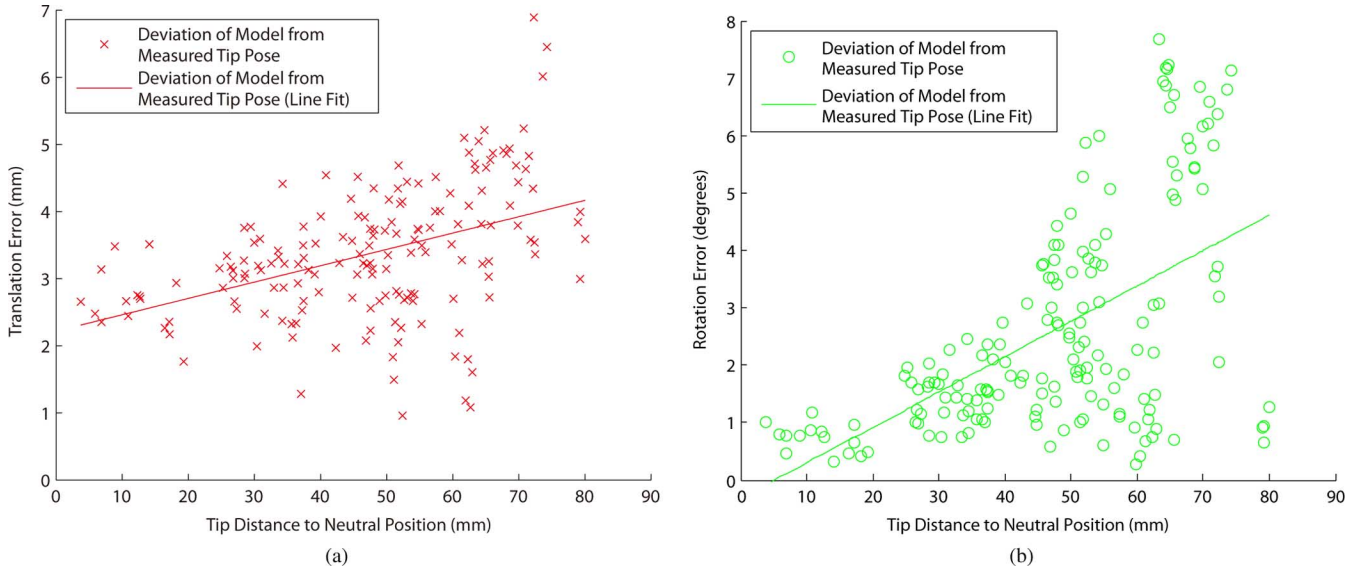


Fig. 9. Validation of the transducer tip model. In relation to the distance of the tip from its neutral position (in millimeters), we compared 171 tip poses not used for model generation to their corresponding poses computed via the model, in terms of (a) their translation difference in millimeters and (b) their rotation difference in degrees. For example, for the tip pose represented by the first data point on the x axis, the transducer tip is bent 3.7 mm away from its neutral position, and we measured a deviation of 2.7 mm and 1.0° from the modeled pose.

marker and one magnetic sensor each rigidly attached to the transducer shaft.

Intraoperatively, every measured pose of the magnetic sensor on the shaft is transformed by applying (1). The error corresponding to the transformation is computed using (2), considering the translation error δ_{trans} or the rotation error δ_{rot} only, or a combination of both (δ). The respective error can be used as a distrust value, which is compared to a selectable threshold to reject data of the magnetic sensor on the tip as probably distorted. The surgical staff can be automatically warned of possible errors.

b) Error Correction: As the magnetic sensor on the shaft is in close proximity to the one on the tip, both sensor measurements will most likely be affected by any magnetic field distortions. As long as the main error component measured at both sensors is the same, it may also be partially corrected like static field distortions. A simple approach to approximate a correction of erroneous measurements is to transfer deviations detected at the magnetic sensor on the shaft to the one on the tip: We can compute the distortion of the measurements on the shaft ${}^{\text{EMT}}R_{\text{MS}_{\text{shaft}}(\text{meas})}$ and undo this distortion on the tip provided that the distortion field is fairly constant for the two sensors. As the sensors can be rotated relative to each other we need to compute this distortion relative to the fixed OT (world) coordinate frame.

Therefore, the rotational and translational parts of the deviation between the previously calibrated (“calib”) and the currently measured (“meas”) transformation on the shaft can be applied to the measured transformation on the tip to obtain corrected (“corr”) transformations

$$\begin{aligned} & {}^{\text{OT}}R_{\text{MS}_{\text{tip}}(\text{corr})} \\ &= {}^{\text{OT}}R_{\text{MS}_{\text{shaft}}(\text{meas})}^T \cdot {}^{\text{OT}}R_{\text{MS}_{\text{shaft}}(\text{calib})} \\ & \quad \cdot {}^{\text{OT}}R_{\text{MS}_{\text{tip}}(\text{meas})} \end{aligned} \quad (6)$$

$$\begin{aligned} & {}^{\text{OT}}t_{\text{MS}_{\text{tip}}(\text{corr})} \\ &= -{}^{\text{OT}}t_{\text{MS}_{\text{shaft}}(\text{meas})} + {}^{\text{OT}}t_{\text{MS}_{\text{shaft}}(\text{calib})} \\ & \quad + {}^{\text{OT}}t_{\text{MS}_{\text{tip}}(\text{meas})}. \end{aligned} \quad (7)$$

2) Model-Based Approach: Dynamic field distortions, caused by e.g., moving instruments close to the sensors, are particularly difficult to reproduce, because the variation in field strength is usually not shift invariant (i.e., disturbances affect the field strength nonuniformly at different locations) as already described by [20] and [21]. Hence the magnetic field at the sensor on the shaft is often distorted in a completely different direction and magnitude than at the sensor on the tip, even though the sensors are placed close to each other. This makes the simple, redundancy-based error estimation approach unreliable (for experimental results, refer to Sections IV-E and IV-F).

a) Error Detection: Another, more sophisticated approach for error estimation requires a previous calibration and modeling of the possible transducer tip movements (see Section III-A5). In the absence of distortions, the measurements of the magnetic sensor on the tip can be assumed to lie on the previously modeled cardioid of revolution-like shape, reducing their DOF from six to two (ϕ and ψ). Because the true motion of the tip is constrained to those two DOF, we can exploit the redundancy of the remaining four DOF. If measurements do not lie exactly on the cardioid of revolution-like surface, we can deduce poses similar to the measurements but lying on the surface that are likely to be closer to the true pose of the sensor.

The model is built relative to the optical marker, which is attached to the transducer shaft, and is not influenced by magnetic field distortions. Therefore, only the previously determined static transformation ${}^{\text{OM}_{\text{shaft}}}T_{\text{MS}_{\text{shaft}}}$ and the tip model parameters (compare Section III-A5) are needed when optimizing ψ and ϕ by the Levenberg–Marquardt algorithm.

After optimization of the model angles ϕ and ψ , we can compute the remaining distance between the modeled and the un-

corrected pose of the magnetic sensor attached to the tip. With a perfect model in an error-free environment it would always be possible to find model angles ϕ and ψ such that the modeled pose is identical to the uncorrected pose. Thus, a deviation between these two poses can be used as a distrust value in order to warn the surgical staff about detected distortions.

b) Error Correction: For error correction, we simply replace the measured, uncorrected pose of the sensor attached to the tip with the pose on the modeled surface that was previously computed to be closest to the distorted pose.

3) Vision-Based Correction: As the intrinsic and extrinsic camera parameters of the laparoscope and hence the spatial location of the image plane are known, another approach to improve the tracking accuracy of the magnetic sensor mounted on the tip is to automatically localize the transducer tip in the images of the laparoscope camera and adjust the measured sensor pose by an in-plane transformation accordingly. This correction transformation can further improve the results of the model-based error correction method, especially in correcting errors introduced by calibration inaccuracies. For our work on this topic see [24].

In the next section, we describe our evaluation of all system calibration and error estimation methods.

IV. EXPERIMENTAL EVALUATION

The accuracy throughout system calibration and transducer modeling as well as error detection and correction was evaluated in a series of experiments.

Our experimental setup is depicted in Fig. 1. As can be seen on the figure, we temporarily mounted an additional optical marker (made entirely of plastic so as not to influence the EMT) on the flexible transducer tip, below referred to as “OM_{tip}.” Similarly to magneto-optical coregistration, we determined the transformation $^{OM_{tip}}T_{MS_{tip}}$ from magnetic sensor coordinates to optical marker coordinates (see Section III-A3). Along with optical tracking, this transformation $^{OM_{tip}}T_{MS_{tip}}$ can be used as a reference method for determining the pose of the magnetic sensor on the tip. The method is of course not applicable to a clinical setting because of the additional optical marker at the flexible transducer tip, but it can be used well for comparison of accuracy.

A. Laparoscope Camera and Laparoscopic Ultrasound Calibration

Laparoscope camera calibration was studied extensively in our prior work [26], which yielded 2-D overlay rms error of about 1.6 mm for C-arm CT data (for further results obtained in the current setup, refer to Section IV-F2). Laparoscopic ultrasound calibration was also assessed previously by imaging a magnetic sensor submerged in a water bath and comparing its appearance in the ultrasound plane with the tracking data [23]. Because the spatial location of the ultrasound plane is known, we can compute a 3-D position for the appearance of the sensor there and compute the difference to its tracked position. This resulted in 3-D rms error of about 1.7 mm.

TABLE I

MAGNETO-OPTICAL CO-REGISTRATION RESIDUAL ERRORS BEFORE AND AFTER OPTIMIZATION. FOR THE COMPUTATION OF δ SEE (1). MINIMUM, MEAN, SD, RMS VALUE, AND MAXIMUM ARE GIVEN FOR EACH CASE

	Min	Mean	SD	RMS	Max
Before optimization					
Translation in mm (δ_{trans})	1.67	2.56	0.45	2.60	3.41
Rotation in degrees (δ_{rot})	0.56	1.04	0.18	1.06	1.44
δ	4.28	5.69	0.71	5.73	7.11
After optimization					
Translation in mm (δ_{trans})	0.33	1.19	0.48	1.29	2.05
Rotation in degrees (δ_{rot})	0.03	0.87	0.22	0.89	1.37
δ	2.12	3.79	0.70	3.85	5.70

TABLE II

ROC KEY FIGURES FOR PREDICTION OF TRACKING ERRORS OF AT LEAST 2.5, 5.0, AND 7.5 MM. THE AREA UNDER CURVE (AUC), MAXIMUM YODEN INDEX (J_{max}), BEST THRESHOLD, TRUE POSITIVE RATE (TPR), SPECIFICITY (SPC), MINIMUM FALSE POSITIVE (FP_{min}), AND MAXIMUM FALSE NEGATIVE (FN_{max}) ARE GIVEN FOR EACH CASE

	AUC	J_{max}	Threshold	TPR	SPC	FP_{min}	FN_{max}
2.5 mm							
Redundancy-based	0.67	0.26	5.64	0.50	0.75	0.86	12.52
Model-based	0.93	0.70	3.14	0.91	0.79	1.26	4.67
5.0 mm							
Redundancy-based	0.73	0.37	6.08	0.62	0.75	0.86	12.52
Model-based	0.97	0.84	6.53	0.91	0.93	2.85	8.37
7.5 mm							
Redundancy-based	0.82	0.52	7.02	0.73	0.78	0.86	14.29
Model-based	0.98	0.84	8.37	0.96	0.89	4.64	9.93

B. Magneto-Optical Coregistration

When coregistering the EMT and the OT we determine the transformations $^{OM_{shaft}}T_{MS_{shaft}}$ from the magnetic sensor to the optical marker on the transducer shaft and $^{OM_{EMT}}T_{EMT}$ from the EMT coordinate frame to its attached optical marker. Because of tracking errors it is not possible to find an exact solution for both transformations, only the optimal solution. At all poses which were used for registration, an rms residual error of $\delta_{trans} = 1.29$ mm for translation and $\delta_{rot} = 0.89$ degrees for rotation remained after optimization [see Section III-A3, (2)]. For detailed results before and after optimization see Table I.

For verification of the coregistration accuracy, we conducted a series of independent registrations, each performed with multiple transducer poses. At least 13 poses belonging to the same registration were used to verify the accuracy of the respective previous registration. This was done while the transducer tip remained in an approximately neutral position, with only minor movements due to gravitational force. In a second series, we fixed the transducer shaft at one position and moved the transducer tip to all selectable poses using the levers. This was repeated for multiple other transducer shaft poses.

Applying (1) and (2), for each pose we calculated the translation error δ_{trans} and the rotation error δ_{rot} for the magnetic sensor on the shaft. Replacing MS_{shaft} by MS_{tip} and OM_{shaft} by OM_{tip} in these equations, we were also able to compute the errors for the magnetic sensor on the tip in a similar fashion. Table III shows the results.

As can be seen in Table III, the error at the sensor on the shaft is significantly higher than at the sensor on the tip. We attribute this to the larger distance between magnetic sensor and optical marker: The mean orientation error of the sensor on the shaft

TABLE III
3-D TRANSLATION AND ROTATION ERRORS IN AN UNDISTORTED AND A DISTORTED MAGNETIC FIELD. MINIMUM, MEAN, SD, RMS VALUE, AND MAXIMUM ARE GIVEN FOR EACH CASE. FOR A GRAPHICAL COMPARISON SEE FIG. 12

3D errors	Translation (mm)					Rotation (degrees)				
	Min	Mean	SD	RMS	Max	Min	Mean	SD	RMS	Max
Undistorted magnetic field										
Magnetic sensor (shaft)	1.10	2.66	1.19	2.91	5.09	0.31	1.10	0.34	1.15	1.85
Magnetic sensor (tip)	0.10	1.03	0.77	1.28	3.54	0.16	0.50	0.26	0.56	1.24
Redundancy-based correction	0.75	2.72	1.09	2.92	5.89	0.44	1.18	0.46	1.26	2.25
Model-based correction	1.06	2.22	0.48	2.27	2.90	0.18	0.82	0.33	0.88	1.62
Distorted magnetic field										
Magnetic sensor (shaft)	0.95	6.86	4.84	8.39	24.14	0.25	2.71	1.99	3.36	9.01
Magnetic sensor (tip)	0.82	5.47	4.23	6.91	24.10	0.08	2.52	1.99	3.21	10.40
Redundancy-based correction	0.59	5.73	3.42	6.67	19.85	0.28	4.36	3.14	5.37	14.36
Model-based correction	0.47	2.72	1.59	3.15	9.65	0.18	2.77	1.93	3.37	10.38

is 1.10° . In practice, this error only partly results in an additional position error, but theoretically, over the estimated distance of 366 mm from the magnetic sensor to the optical marker on the transducer shaft, for every 0.1° , there may be an additional position error of 0.6 mm. At the sensor attached to the tip the same effect would only cause an additional position error of 0.07 mm because of the much smaller distance.

C. Transducer Axis Calibration

During axis calibration the rms residual error of one calibration, i.e., the distance of the collected position measurements from the optimized cylinder surface, ranges from 0.57 to 1.03 mm with a mean value of 0.74 mm using 1.3 mm sensors (performing six calibrations). We also inserted a 1.8 mm Ascension sensor into the end of the plastic cylinder instead of a 1.3 mm sensor. This sensor yielded better results of 0.23–0.80 mm with a mean value of 0.42 mm (performing four calibrations).

D. Transducer Tip Modeling

We experimentally evaluated three important errors related to the transducer tip motions: the residual error during computation of the model, the residual error using the computed model, and the repositioning error (independent of the model).

First, we estimated the remaining residual error of the poses used for computation of the model parameters (see Section III-A5). For models determined from five pose sets the rms error ranges from 0.58 to 1.28 mm with a mean value of 0.94 mm for translation and from 3.48° to 3.89° with a mean of 3.66° for rotation.

We next verified the accuracy of the model for another 171 poses that were not used for computation of the model (see Fig. 9). We measured the deviations of the poses from the theoretical model curve in relation to the distance of the tip from its neutral position; a distance of about 75 mm corresponds to at least one of the two steering levers pulled to its maximum position. The rotation error stayed approximately the same (rms was 3.22°), but the translation error was higher (rms 3.50 mm).

We assume the higher translation error to be due to the fact that the bending region of our ultrasound transducer proved to be not ideally elastic, i.e., a slight translation within one of the links of the bending region or a rotation around the instrument axis can still occur, which is not modeled by the current design. Particularly when bending the transducer tip to extreme poses,

the bending region is exposed to large mechanical pulling forces that could cause an additional translation or rotation of the tip. During our experiments, a Bowden cable broke twice when we pulled the two levers to extreme positions, so it seems that the bending region is not designed for such positions. We also received a report from our clinical partner that intraoperatively the transducer is maximally bent away from its neutral position by only about 50 mm.

In a third experiment, we estimated the repositioning accuracy of the transducer tip. We repeatedly moved the two steering levers to the same position and acquired measurements of the transducer tip using the temporarily attached optical marker. To find out whether the order of selection of the control levers influences the positioning repeatability as well, we also alternated the order of selection of the control levers, e.g., first pulled the left lever twice and then pulled the right lever once, or first pulled the right lever once and then pulled the left lever twice. For each of four different final lever positions, we computed the mean tip position and the distances from this mean position. Averaging over the four series, we obtained a mean distance of 1.32 mm from the mean tip position with a standard deviation (SD) of 1.02 mm, minimum of 0.36 mm, and maximum of 3.76 mm. Independently comparing the two orders of selection of the control levers, we obtained a mean distance of 0.56 mm between the first and the second final tip position. So we assume that the overall repositioning variance is much more significant than the variance induced by an alternating order of selection of the steering levers. The overall repositioning variance obtained supports our assumption of the nonideal elasticity of the bending region.

E. Error Detection

For the evaluation of the error detection methods, we recorded 517 distorted measurements, using a knife, a steel rod 10 mm in diameter, and a power supply unit to create varying distortions of the magnetic field. We could not identify their exact grade of steel, but both the knife and the steel rod were attracted to a magnet (in a similar way). The power supply unit was heavily attracted despite being turned off. The knife and steel rod were arbitrarily placed at a distance of about 3–10 cm from the transducer tip, sometimes interposed between the magnetic field generator and the magnetic sensors, but most times not in the direct path between sensors and generator. The power supply unit was placed next to the field generator at a distance of about 30 cm, never in the direct path between sensors and generator.

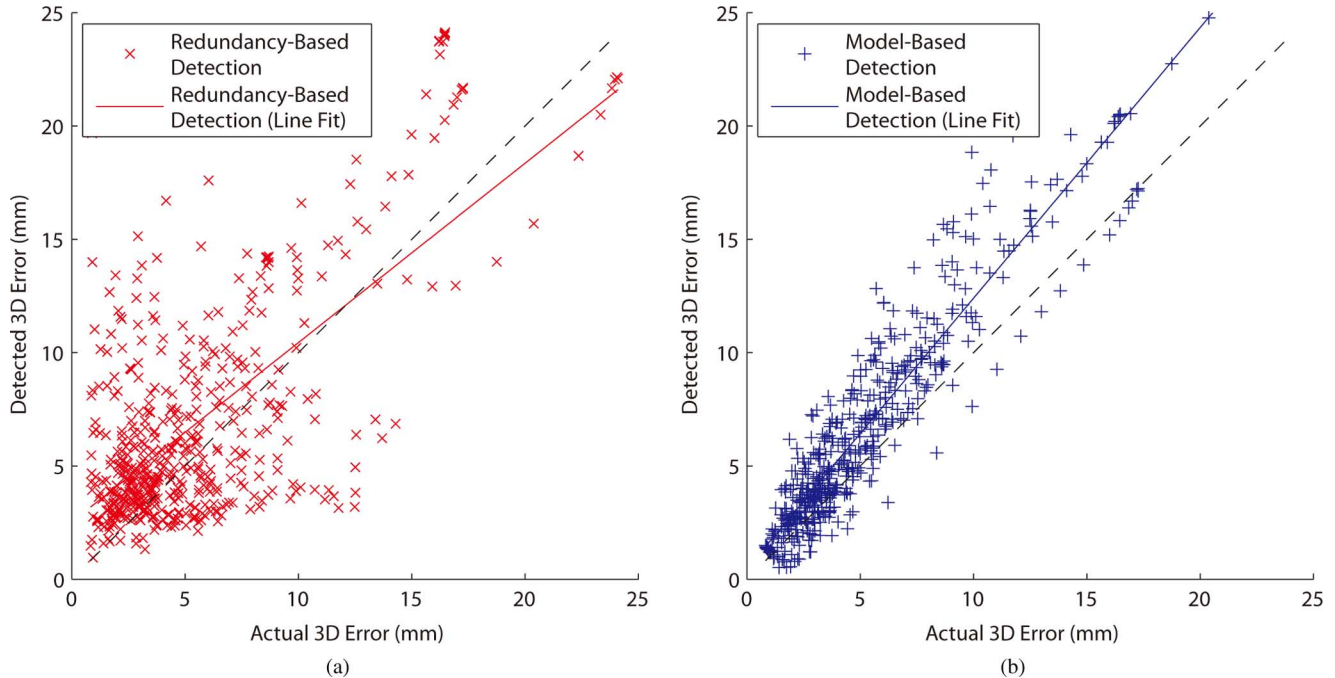


Fig. 10. Comparison of the detected magnitudes of error—using (a) the tracking redundancy-based approach and (b) the model-based approach—to the actual error of the magnetic sensor on the tip (translation in millimeters in all cases). The actual error was determined via an additional optical marker temporarily attached to the transducer tip only during our experiments. The identity function of the actual error is plotted as a dashed line to aid visual comparison. Our comparison shows that errors detected by the model-based approach correlate better with the actual errors.

For each measurement we computed the translation from the position of the magnetic sensor attached to the shaft (as measured via electromagnetic tracking, ${}^{OM_{EMT}}T_{EMT}$, and optical tracking) to its reference position (as computed via ${}^{OM_{shaft}}T_{MS_{shaft}}$ and optical tracking), which reflects the magnitude of error detected by our tracking redundancy-based approach. We also determined the translation from the position of the magnetic sensor on the tip (as measured via the electromagnetic tracking, ${}^{OM_{EMT}}T_{EMT}$, and optical tracking) to its modeled position, which reflects the error detected by our model-based approach. In an ideal and error-free setting both translations would be zero. Additionally, we computed the actual error of the magnetic sensor on the tip, i.e., the translation from the measured position to the reference position (as computed via ${}^{OM_{shaft}}T_{MS_{shaft}}$ and optical tracking), and compared it to both the errors detected by the redundancy-based approach and the model-based approach. Fig. 10 depicts this comparison.

1) *Correlation Coefficient*: Both magnitudes of errors detected by the redundancy-based approach and the model-based approach correlate with the actual error of the magnetic sensor on the tip. As can be seen from Fig. 10, the magnitude of error detected by the redundancy-based approach has a much lower correlation with the actual error (correlation coefficient 0.69) than the one detected by the model-based approach (correlation coefficient 0.95).

2) *Receiver Operating Characteristic*: For both the redundancy-based approach and the model-based approach we can choose a certain threshold value and predict a distortion of the pose of the sensor on the tip if the detected magnitude of error exceeds this threshold.

When predicting distortions, two sorts of errors are possible (explained here for the redundancy-based method, the model-based methods follows similarly): A false positive (type 1 error) occurs when the distance between the calibrated pose and the measured pose of the magnetic sensor on the shaft is above the threshold, but the measurement of the sensor on the tip is actually not distorted, i.e., we erroneously reject data. A false negative (type 2 error) occurs when tracking data of the sensor on the tip is distorted, but the distance between the calibrated and measured pose of the sensor on the shaft is below the threshold, i.e., we fail to predict the distortion. Similarly, we call correctly predicted errors “true positive” and correctly predicted absence of error “true negative.” Note that the error of magneto-optical coregistration is quite large (see Section IV-B) at the sensor on the shaft, so setting a low threshold value will likely trigger false positives.

For our set of distorted measurements we computed several receiver operating characteristics (ROC) for predicting errors of 2.5, 5.0, and 7.5 mm.

Our error prediction is a classifier that computes a distrust value for the current measurement and then decides whether the measurement should be considered erroneous or not. The computation of the distrust value is fixed [see (2)], but the threshold for comparison can be varied. Instead of picking only several exemplary thresholds, for all possible thresholds the false positive rate and true positive rate are computed and combined to form a curve. The ability of the redundancy-based and the model-based methods to predict erroneous measurements of the position of the magnetic sensor attached to the tip is shown in Fig. 11.

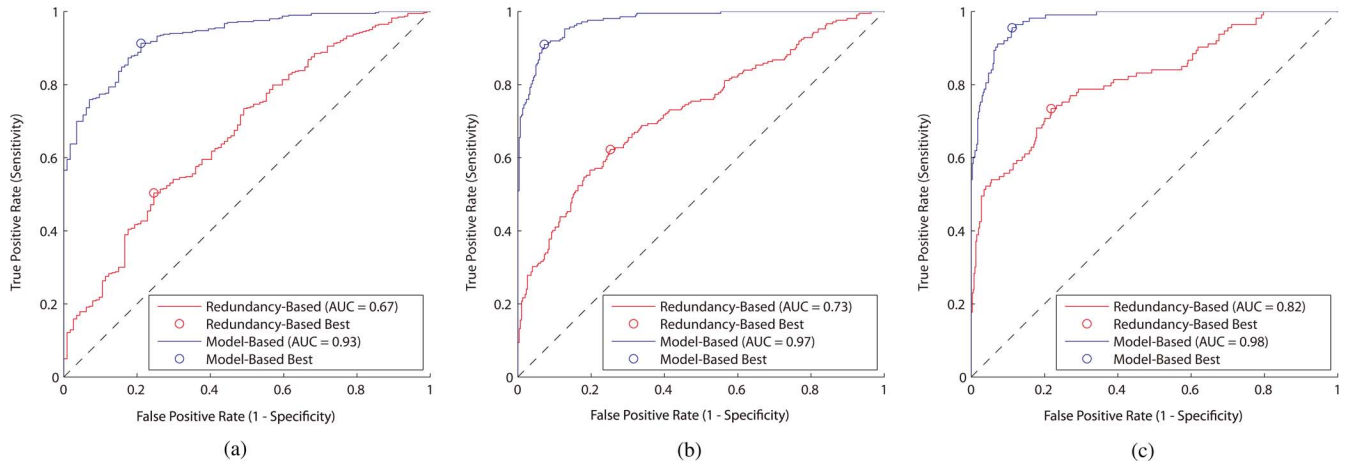


Fig. 11. ROC curves for prediction of tracking errors of at least 2.5, 5.0, and 7.5 mm. Each point on the curve represents the achievable performance for a certain threshold, i.e., sensitivity (true positive rate) and specificity (1—false positive rate). The point with the highest sum of sensitivity and specificity (highest Youden index) has been marked for each curve and may be considered the achievable performance of our error-detection method for each case. (a) 25 mm. (b) 5.0 mm. (c) 7.5 mm.

We considered the value with maximum Youden index [42] to be the optimal choice for a threshold. The Youden index for a given threshold is defined as follows:

$$J = \frac{ad - bc}{(a + b)(c + d)} = \underbrace{\frac{a}{a + b}}_{\text{Sensitivity}} + \underbrace{\frac{d}{c + d}}_{\text{Specificity}} - 1 \quad (8)$$

where a is the fraction of true positives, b the fraction of false negatives, c the fraction of false positives, and d the fraction of true negatives. The possible range of values is from zero to one inclusive.

In Table II we present the key figures for each ROC: For both prediction methods the area under the ROC curve (AUC) and the maximum Youden index J_{\max} have been computed. Additionally, corresponding to J_{\max} , the threshold value, sensitivity (true positive rate, TPR) and specificity (SPC = 1 – FPR, false positive rate), and both the smallest false positive value FP_{\min} and the greatest false negative value FN_{\max} are given. The latter define the most extreme cases where the classifier would have made a wrong decision.

For predicting an error of 2.5 mm or greater, redundancy-based error prediction would in the best case have achieved a sensitivity of 50% and a specificity of 75%. That is, it would have been able to correctly predict 50% of all errors of 2.5 mm or greater and correctly predict 75% of the cases in our data set, where the error was below 2.5 mm. In comparison, the model-based error prediction would have achieved a sensitivity of 91% and a specificity of 79% for the same data.

For predicting an error of 5.0 mm or greater, sensitivity and specificity would have been 62% and 75% (redundancy-based) versus 91% and 93% (model-based). For all values including those for 7.5 mm, see Table II.

The model-based error prediction worked much more reliably. For example when trying to predict an error of 2.5 mm or greater, it would have correctly identified all error-free measurements better than 1.26 mm and all errors above 4.67 mm.

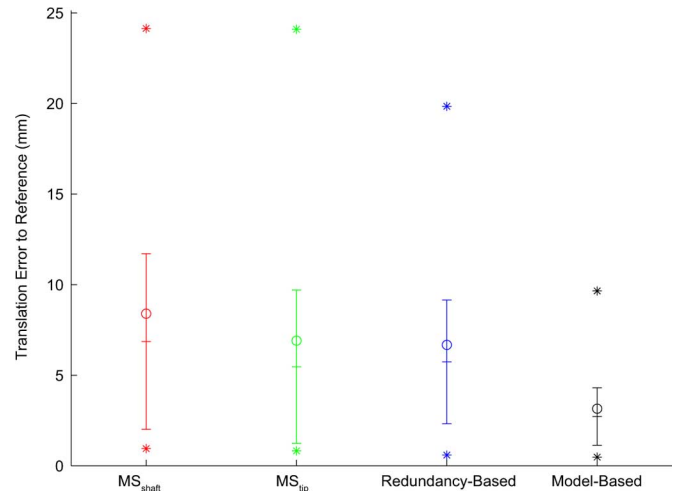


Fig. 12. 3-D translation errors in a distorted field. To distort the magnetic field, we used either a knife, a steel rod, or a power supply unit, while the transducer was fixed in varying locations. In each column, minimum and maximum are represented by stars, the rms error by a circle, and mean and SD by bars. See Table III for exact values including rotation and measurements in an undistorted field.

F. Error Correction

Error correction accuracy was determined in two steps: first, we assessed the 3-D tracking accuracy of the system with and without our proposed error correction methods in comparison to reference measurements obtained via ${}^{OM}_{tip}T_{MS_{tip}}$ and optical tracking. Second, we measured the 2-D overlay accuracy in an application-specific setting, i.e., superimposition of a laparoscope camera image (see [23] and [24] for further details on our application). Three-dimensional points can be projected onto the camera image plane once the projective geometry of the camera is known. The overlay error is the difference between the computed 2-D location of the point projected onto the image plane and the actual location as extracted from the video image.

The two steps cover different aspects: the tracking error is especially relevant for applications like 3-D ultrasound, while the

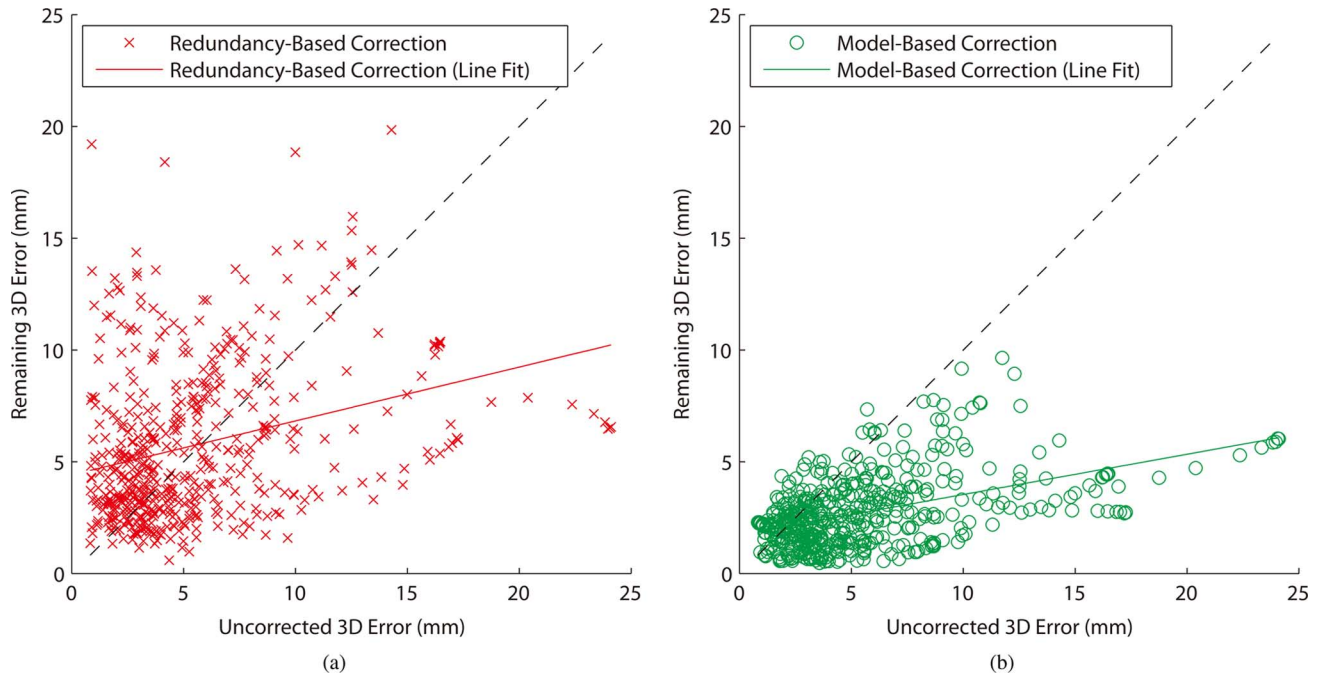


Fig. 13. Performance of (a) tracking redundancy-based error correction and (b) model-based error correction. The error remaining after correction is plotted against the uncorrected error (translation in millimeters in all cases). The dashed line represents the original error without correction and has been added to aid visual comparison.

overlay error is crucial e.g., for medical augmented reality applications. The latter additionally includes the camera calibration error and may be partially corrected using the vision-based correction approach presented in our previous work [24], either exclusively or in combination with the error correction approaches described here.

1) *3-D Accuracy*: When evaluating the performance of the magneto-optical co-registration, at the same time we evaluated the effectiveness of our proposed error correction approaches.

For best possible comparison we assessed all errors simultaneously. We recorded 30 undistorted and 517 distorted measurements, applied both the simple tracking redundancy-based error correction (see Section III-B1) and the model-based error correction (see Section III-B2), and recorded all distances to a reference pose computed using ${}^{OM}_{tip}T_{MStip}$ and optical tracking.

For the model-based error correction approach, the position difference of the modeled to the measured pose of the magnetic sensor on the tip (in millimeters) and the corresponding orientation difference (in degrees) were weighted 1:3 [see (1)].

In the undistorted setting (see Table III) the magnetic sensor on the tip had an rms error of 1.28 mm, the one on the shaft had an rms error of 2.92 mm, and the tracking redundancy-based error correction and the model-based error correction had rms errors of 2.91 and 2.27 mm, respectively.

The tracking redundancy-based error correction performed almost exactly like the sensor on the shaft itself (for rotation it performed slightly worse). The model-based error correction performed better, although it was anchored to the optical marker on the shaft and part of the corresponding magneto-optical coregistration error presumably propagated into it.

In the distorted case (see Fig. 12 and Table III) the model-based error correction with an rms error of 3.15 mm clearly out-

performed the simple tracking redundancy-based approach with an rms error of 6.67 mm. Model-based error correction proves to be functional, as the uncorrected measurements of the magnetic sensor on the tip had an rms error of 6.91 mm. The orientation error, however, could not be improved (rms 3.21° uncorrected and 3.37° corrected). This suggests that either the orientation difference to the uncorrected sensor should be weighted more heavily than it is now, or that the model should be extended to better approximate rotation of the transducer tip.

For a comparison of both error correction approaches see Fig. 13. Whereas the simple tracking redundancy-based error correction had a much wider variance as well as a poorer overall performance, the model-based error correction in most cases could reduce the translation error to below 5 mm, even for original errors in the centimeter range.

However, probably due to the propagation of errors from tracking, calibration, and modeling, for errors lower than approximately 2.1 mm the model seems to give slightly worse results than the uncorrected measurements of the sensor on the tip. The model-based error correction could thus be restricted to cases where a relatively high error is predicted (for error prediction see Section III-B2a).

2) *2-D Overlay Accuracy*: For assessing the overlay accuracy in both the undistorted and distorted case, the ultrasound transducer was fixed in various poses and the laparoscope was used to observe the transducer tip from various angles and distances.

In the course of the experiments the transducer tip was steered to different angles and the laparoscope was also rotated around its own axis. For distorting the magnetic field we again used the steel rod with a diameter of 10 mm.

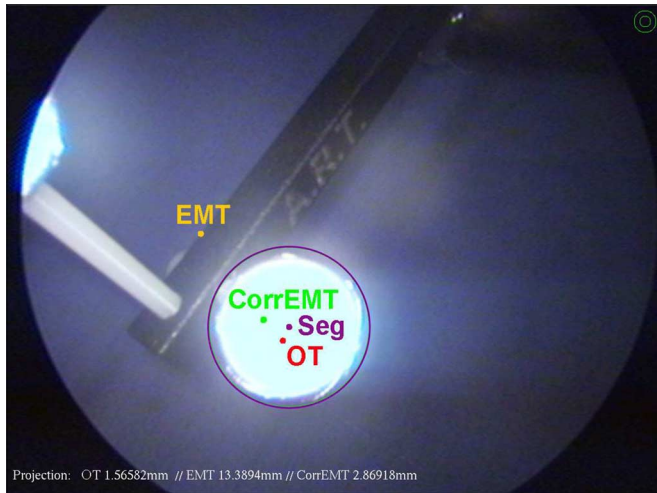


Fig. 14. Automatic segmentation of one retro-reflective sphere of the optical marker attached to the tip and projection of the position of the magnetic sensor on the tip determined via various methods. Here, “Seg” refers to the position of the segmented sphere, “OT” to the projection of the pose of the optical marker attached to the tip centered in the sphere, “EMT” to the projection of the uncorrected position of the magnetic sensor on the tip, and “CorrEMT” to the projection of a corrected position of the sensor on the tip (corrected by one of the above-mentioned methods). The metal rod was placed at a distance of about 5 cm from the magnetic sensors to disturb the magnetic field. The image was enhanced for readability.

Using the transformation $OM_{tip}T_{MS_{tip}}$ from the magnetic sensor to the optical marker on the tip, at each measurement we transformed

- 1) the uncorrected position of the magnetic sensor attached to the tip (“ MS_{tip} ”);
- 2) the tracking redundancy-based corrected position of the sensor on the tip (“CorrRedundancy”);
- 3) the model-based corrected position of the sensor on the tip (“CorrModel”).

The resulting positions were then projected into the image plane, the spatial location of which was known from camera calibration. The measured 3-D position of the optical marker on the tip (centered in one of the retro-reflective spheres) was also projected into the image plane, as shown in Fig. 14. The distance in millimeters parallel to the image plane to the segmented midpoint of the sphere was computed and taken as the measure for overlay accuracy.

Only measurements within a distance of 5–20 cm between the sphere and the camera center were accepted. This rather large distance of up to 20 cm is required to observe both the transducer tip (for axis segmentation) and the sphere at the same time. Keeping such a large distance is however very unlikely during surgery, for which the laparoscope was calibrated for a maximum working distance of only about 10 cm. This reduces the overlay accuracy when the laparoscope is further away than 10 cm, so theoretically the results obtained here could be further improved.

In our previous experiments [23], we used the steel rod to create dynamic distortions similar to those from surgical instruments, and a metal plate to create static distortions similar to an operating table. At the time of these experiments, only the

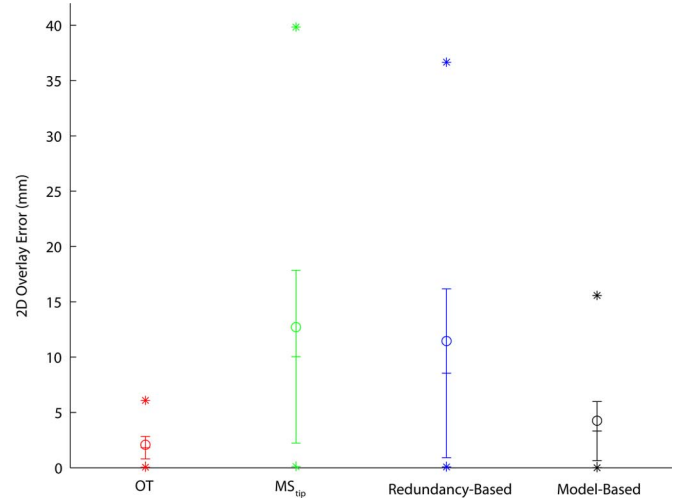


Fig. 15. 2-D overlay errors in a distorted magnetic field. In each column, minimum and maximum are represented by stars, the rms error by a circle, and mean and SD by bars. See Table IV for exact (including undistorted) values.

TABLE IV
OVERLAY ERRORS IN AN UNDISTORTED AND A DISTORTED
MAGNETIC FIELD. MINIMUM, MEAN, SD, RMS VALUE,
AND MAXIMUM ARE GIVEN FOR EACH CASE

2D overlay errors	Translation (mm)				
	Min	Mean	SD	RMS	Max
Undistorted magnetic field					
Projected OT	0.11	2.67	1.38	3.00	7.57
Projected EMT (MS_{tip})	0.17	3.57	2.49	4.35	11.81
Redundancy-based correction	0.38	3.73	1.99	4.23	11.19
Model-based correction	0.15	2.25	1.39	2.64	7.99
Distorted magnetic field					
Projected OT	0.05	1.81	1.02	2.08	6.10
Projected EMT (MS_{tip})	0.11	10.03	7.81	12.71	39.84
Redundancy-based correction	0.07	8.55	7.63	11.45	36.66
Model-based correction	0.01	3.32	2.67	4.26	15.58

tracking redundancy-based error correction method was available and the results were not yet promising: in an undistorted environment, the accuracy of the corrected sensor was sometimes poorer than the uncorrected measurements. Dynamic distortions got worse in most cases and only static distortions could be partially corrected; errors in the centimeter range still remained.

To assess the overlay accuracy of the new, improved error correction methods we took 207 undistorted and 935 distorted measurements. For the results in undistorted and distorted cases see Fig. 15 and Table IV. As illustrated, the simple tracking redundancy-based error correction also performed insufficiently in the new 2-D experiments, whereas the model-based approach yielded major improvements compared to the uncorrected measurements.

Combining the model-based error correction with the vision-based method described in our previous work [24] (see also Section III-B3) yielded even better performance than the model-based method alone. In the scatterplot of Fig. 16 you can see a comparison of the error correction performance of

- the simple tracking redundancy-based error correction method;
- the model-based error correction method;

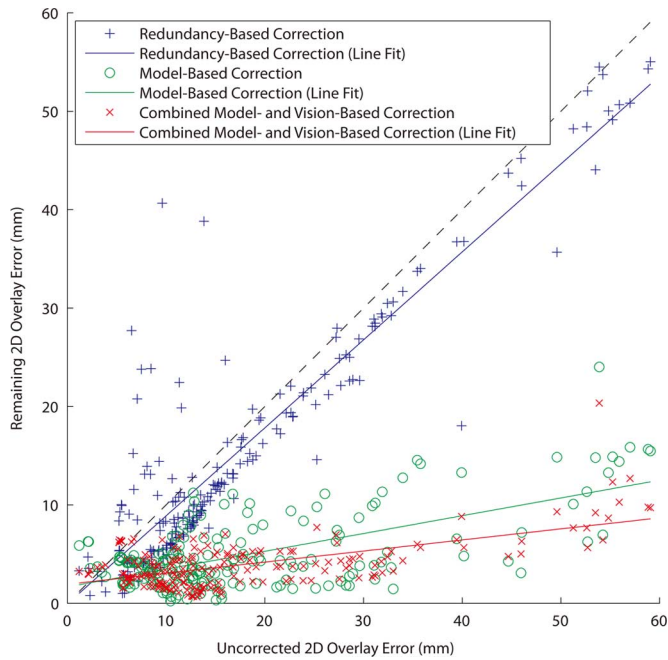


Fig. 16. Performance of the different error correction methods, measured in 2-D perpendicular to the viewing direction. The error remaining after each correction is plotted against the uncorrected error (translation in millimeters in all cases). The dashed line represents the original error without correction and has been added to aid visual comparison.

- a combination of the model-based and vision-based error correction methods.

V. DISCUSSION

As corroborated by our clinical partner, accuracy requirements in abdominal (laparoscopic) surgery are different than in e.g., orthopedic surgery or neurosurgery. A discrimination of about 5 mm is usually sufficient, since canalicular structures such as vessels and bile ducts play a critical role if they are 5 mm or thicker in width. A lymph node is considered to be inflicted by a tumor if the diameter is more than 10 mm. Accordingly, the measurements obtained for the undistorted case as well as for the distorted case after model-based error correction, both of which yielded rms error below 5 mm, are certainly acceptable under clinical conditions.

Our results show that the model-based approach is clearly superior to the redundancy-based method for error correction as well as for error detection. This section presents a comparison of our methods and results to related work. We investigate the differences and suggest possible directions for future research.

A. Error Detection

The authors in [20] and [21] mentioned that the variation in field strength is usually not shift invariant, i.e., two sensors mounted a certain distance apart are affected differently by magnetic field distortions. While this is essential for their error detection methods, it significantly impacts our proposed redundancy-based error detection and correction method.

Both [20] and [21] fix two magnetic sensors rigidly to each other and determine the distance between them in a

TABLE V
DETECTION RATE OF ERRORS GREATER THAN 1 MM FOR DIFFERENT THRESHOLDS $\Delta_{\text{det_thresh}}$, AS PRESENTED IN [20]. IF $\Delta_{\text{det_thresh}}$ IS EXCEEDED, THE SYSTEM IS CONSIDERED TO BE DISTORTED

$\Delta_{\text{det_thresh}}$	0.5	1.0	1.5	2.0
Detection rate (in %)	87	67	39	28

TABLE VI
CORRELATION BETWEEN THE MEASURING ERROR p AND THE PLAUSIBILITY VALUE FOR DIFFERENT INSTRUMENTS, AS DESCRIBED IN [21]. p IS THE KNOWN DEVIATION OF THE MEASURED TOOL TIP POSITION FROM ITS ACTUAL POSITION, THE PLAUSIBILITY VALUE REFLECTS THE CALCULATED DEVIATION. p_{max} DENOTES THE MAXIMUM KNOWN DEVIATION OBTAINED IN ONE EXPERIMENT

Experiment	Forceps	Shaver	Endoscope
Correlation (%)	94	80	49
Max. measuring error p_{max} (mm)	4.7	8.7	1.1

distortion-free environment ([21] applies an additional fixed transformation from each sensor to a calibrated pointer tip before computing the distance, but otherwise the approaches are identical). Then both groups induce various distortions, measure the “movement” of one sensor (its position is actually fixed) and compare it to the measured change in distance between both sensors.

The results of [20] are presented in Table V, where $\Delta_{\text{det_thresh}}$ is the threshold value for the deviation of the distance between both sensors. The system is considered to be distorted if $\Delta_{\text{det}} = \left| \|x_2 - x_1\|_{\text{measured}} - \|r_{\text{Offset}}\|_{\text{known}} \right|$ exceeds $\Delta_{\text{det_thresh}}$, where x_1 and x_2 denote the translational readings from sensor 1 and 2 and r_{Offset} is the known distance between the sensors. Using a threshold of 0.5 mm, a “detection rate” of 87% was achieved, i.e., 87% of all errors greater than 1 mm were correctly detected. Unfortunately a ratio of false positives is not provided, so a direct comparison to all our results is not possible.

[21] used different instruments to induce distortions of the magnetic field, as shown in Table VI. For each instrument it presents the correlation coefficient between the measuring error p and the plausibility value d , where p denotes the known deviation of the measured tool tip position from the actual tool tip position and $d = \|t_2 - t_1\|$ is the difference between the two tool tip positions t_1 and t_2 calculated from the measurements of sensor 1 and 2. For example using a forceps they caused a maximum measuring error p_{max} of 4.7 mm with a correlation coefficient of 94%. Again, a direct comparison to all our results is not possible given only the correlation coefficient.

However, we may assume that our redundancy-based error detection method performed similarly to the results of both [20] and [21], although we faced additional difficulties: the distance between the magnetic sensor and the optical marker on the shaft is rather large (366 mm). On the one hand, this causes a magneto-optical coregistration error of 2.66 mm for the magnetic sensor on the shaft in our setup (see Table III), so low thresholds trigger false alarms easily. On the other hand, our setup has the advantage that the optical tracking of the optical marker on the transducer shaft is not affected by magnetic field distortions.

In contrast to the redundancy-based error detection method, the model-based approach clearly performs better for comparable measures than both [20] and [21]. We are able to achieve a higher sensitivity than [20] and a higher correlation than [21].

For applications in minimally invasive surgery, the methods of [20] and [21] require instruments with a rigid tip where both sensors can be mounted. It would be possible to place two sensors at the tip of our transducer, but the distance between those must not be too small ([20] used 103 mm). Otherwise both sensors might be within an area of similar field deformation and affected too similarly to reliably detect deviations.

B. Error Correction

The redundancy-based error correction did not gain any improvements for the orientation error and only slight improvements for the position error. This suggests that the magnetic sensors on the tip and on the shaft are mounted too far apart, so they are not affected by distortions in a similar enough way.

The model-based error correction did reduce the rms position error from 6.91 to 3.15 mm. The orientation error stayed approximately the same (rms 3.21 versus 3.37). The latter suggests that either the model should be refined to better match the real rotation, probably even including elasticity constraints, or that the difference in rotation to the uncorrected measurements of the magnetic sensor on the tip should be weighted more strongly than it is now. However, there is a trade-off between orientation error and position error: a stronger weighting of the rotation difference to the uncorrected measurements of the sensor can cause the model to favor poses with lower orientation error but higher position error (see Section III-A5). Finding an optimal combination requires further investigation.

There might be limits to the achievable error correction capabilities of the model-based approach: errors are propagated and accumulated through tracking, magneto-optical coregistration, axis calibration, and modeling. Coregistration also introduces additional errors. [14] mentions that in their setup the coregistration of the EMT and the OT alone introduced 0.1–0.2 mm of additional error compared to using the EMT only. Probably even higher errors have to be anticipated for the calibration of the laparoscopic ultrasound transducer shaft, especially because the optical marker and magnetic sensor on the shaft are mounted a large distance apart.

Metal-Immune Electromagnetic Tracking Systems: Magnetic field generators optimized for metal environments were recently presented by NDI and Ascension. Ascension's flat transmitter is designed to overcome distortions from below the field generator, caused e.g., by the operating table. Due to its lower excitation, in our setup it unfortunately performed worse than the midrange transmitter. During ultrasound calibration, we obtained errors of 4–8 mm using the flat transmitter versus 1.7 mm using the mid-range transmitter [23], [24]. Bigger sensors could be used to improve accuracy but this would require bigger trocars. Using 1.3 or 1.8 mm sensors, the total diameter of the transducer could be kept below 12 mm (including sterile cover), so it would still fit a regular trocar. Furthermore, metal-immune systems will not be "immune" from dynamic distortions caused e.g., by moving ferromagnetic instruments close to the sensor or field generator.

One Sensor Setup: It is even possible to abandon the sensor on the shaft entirely. The optical marker on the tip is then also needed for construction of the model, but as in the current setup

it can be removed afterwards. After determining the transformation ${}^{OM_{tip}}T_{MS_{tip}}$ from the magnetic sensor to the optical marker on the tip, it is possible to compute the movement of the magnetic sensor on the tip in relation to the optical marker on the shaft. Instead of using ${}^{EMT}T_{MS_{tip}}$ and ${}^{EMT}T_{MS_{shaft}}$, the model would be constructed from ${}^{OT}T_{OM_{tip}}$, ${}^{OM_{tip}}T_{MS_{tip}}$, and ${}^{OT}T_{OM_{shaft}}$. For axis calibration, however, a calibration phantom would have to be constructed to allow axis calibration using the OT instead of the EMT.

A second option for model construction would be to transform measurements of the magnetic sensor on the tip via the EMT, its attached optical marker, and the OT into the coordinate system of the optical marker on the shaft, i.e., by ${}^{OT}T_{OM_{EMT}}$, ${}^{OM_{EMT}}T_{EMT}$, ${}^{EMT}T_{MS_{tip}}$, and $({}^{OT}T_{OM_{shaft}})^{-1}$. For this method even the optical marker on the tip would not be needed any more. But then the determination of the transformation ${}^{OM_{shaft}}T_{EMT}$ from the EMT to its attached optical marker would require an additional calibration phantom, because for magneto-optical coregistration one magnetic sensor and one optical marker must be fixed in relation to each other. In our opinion this approach would be less favorable, because more tracking and calibration errors may be accumulated during the determination of the model parameters.

No matter which option is chosen, error detection using the model-based approach would be possible in the same manner—without a second sensor and still with superior performance compared to the current state of the art. It should be verified that these assumptions are correct and that our proposed methods also work without an additional sensor mounted on the shaft.

Sensor Fusion: The error correction approach we describe here is based on the exploitation of redundancy in our tracking data. For more complicated setups, where more and different types of information are available, those could be fused using more sophisticated methods like Kalman [43] or Monte Carlo [44] filtering. The additional complexity of approaches like these was not needed in our case but could easily be included, e.g., by using a Kalman filter for smoothing our tracking data.

C. Future Work

Future work should include a quantification of the robustness of the error correction methods proposed in this paper.

The current system has been evaluated thoroughly in a laboratory setup. In future work the integration of the tracking systems into a clinical operating room setup should also be evaluated, e.g., regarding tracker installation and sterilization of tracking bodies and sensors, along with their precise repositioning to laparoscopic instruments. The same holds for the integration of our proposed procedures into the surgical workflow, such as practical calibration and verification procedures and user interfaces for surgical staff. The first goal in particular could be achieved using integrated devices: for instance, the optical tracking cameras could be attached to surgical lights or the operating room ceiling, as done in our previous work [26], while the magnetic field generator could be integrated into the surgical table, like the flat transmitter from Ascension. Magnetic sensors should also be entirely integrated into the laparoscopic instruments so that no dedicated sterilization

procedure is required. Optical markers that can be used in autoclaves are already available from e.g., Brainlab. However, in order to simplify the intraoperative setup process, there is a need for either optical markers that can be very precisely (re-)mounted to the instruments, e.g., using snap-on connections, or adequate routines for a fast intraoperative system calibration.

VI. CONCLUSION

We present new methods for detecting and partially correcting static and dynamic magnetic tracking errors. They are applied to a flexible laparoscopic ultrasound transducer which is localized by a hybrid magneto-optical tracking system. Our new evaluation methodology uses an optical marker as a reference and closes the chain of transformations between optical tracking, electromagnetic tracking, laparoscope images, and the marker. This provides a sound validation of the proposed methods against reference data obtained from optical tracking.

The methods presented could improve navigation in a large set of minimally invasive procedures where flexible laparoscopic ultrasound or similarly constructed surgical instruments with known mechanical properties of their bendable tips are used, e.g., for liver, biliary tract, and pancreas interventions. A setup with these flexible instruments requires only a single calibration routine, which can be done offline and remains valid until the sensors are repositioned.

The novel model-based approach improves the error detection of [20] and [21] so that navigation systems based on magnetic tracking can discover these uncertainties fully automatically and reliably, and take them into account for proper visualization and feedback during the intervention.

Many researchers have worked on the correction of static electromagnetic errors and the detection of dynamic electromagnetic errors. However, to the authors' knowledge none of them have addressed the *online and real-time reduction of dynamic electromagnetic errors* for tracking of laparoscopic ultrasound, which does not need an on-site calibration of the tracking volume.

This work is a step towards reliability within the usage of magnetic tracking, confidence in the technology, and its integration into the localization and navigation of flexible instruments in operating theaters where dynamic magnetic field distortions cannot be entirely eliminated.

ACKNOWLEDGMENT

The authors would like to thank S. Holdstock for proof-reading of the paper. They would also like to thank H. Feussner and A. Schneider from Klinikum rechts der Isar for their great support in all medical questions and for the provision of the laparoscope and the ultrasound transducer.

REFERENCES

- [1] J. J. Jakimowicz, "Intraoperative ultrasonography in open and laparoscopic abdominal surgery: An overview," *Surgical Endoscopy*, vol. 20, pp. 425–435, Mar. 2006.
- [2] B. Rau, M. Hunerbein, and P. M. Schlag, "Is there additional information from laparoscopic ultrasound in tumor staging?," *Digestive Surgery*, vol. 19, pp. 479–483, 2002.
- [3] S. Ganguli, J. B. Kruskal, D. D. Brennan, and R. A. Kane, "Intraoperative laparoscopic ultrasound," *Radiologic Clin. North Am.*, vol. 44, pp. 925–935, 2006.
- [4] J. Leven, D. Burschka, R. Kumar, G. Zhang, S. Blumenkranz, X. D. Dai, M. Awad, G. D. Hager, M. Marohn, M. Choti, C. Hasser, and R. H. Taylor, "Davinci canvas: A telerobotic surgical system with integrated, robot-assisted, laparoscopic ultrasound capability," in *Proc. Int'l Conf. Medical Image Computing and Computer Assisted Intervention (MICCAI)*. New York: Springer-Verlag, 2005, vol. 3749, Lecture Notes in Computer Science, pp. 811–818.
- [5] B. P. Lo, A. Darzi, and G.-Z. Yang, "Episode classification for the analysis of tissue/instrument interaction with multiple visual cues," in *Proc. Int'l Conf. Medical Image Computing and Computer Assisted Intervention (MICCAI)*, R. E. Ellis and T. M. Peters, Eds. New York: Springer-Verlag, 2003, vol. 2878, Lecture Notes in Computer Science, pp. 230–237.
- [6] J. Climent and P. Mares, "Automatic instrument localization in laparoscopic surgery," *Electron. Lett. Comput. Vis. Image Anal.*, vol. 4, no. 1, pp. 21–31, 2004.
- [7] S. J. McKenna, H. N. Charif, and T. Frank, "Towards video understanding of laparoscopic surgery: Instrument tracking," *Image and Vision Computing New Zealand*, 2005.
- [8] S. Voros, J.-A. Long, and P. Cinquin, "Automatic localization of laparoscopic instruments for the visual servoing of an endoscopic camera holder," in *Proc. Int'l Conf. Medical Image Computing and Computer Assisted Intervention (MICCAI)*. New York: Springer, 2006, vol. 4190, Lecture Notes in Computer Science, pp. 535–542.
- [9] C. Doignon, F. Nageotte, and M. de Mathelin, "Segmentation and guidance of multiple rigid objects for intra-operative endoscopic vision," in *Workshop on Dynamic Vision, European Conference on Computer Vision*, Graz, Austria, 2006, pp. 314–327.
- [10] J. Ellsmere, J. Stoll, W. Wells, R. Kikinis, K. Vosburgh, R. Kane, D. Brooks, and D. Rattner, "A new visualization technique for laparoscopic ultrasonography," *Surgery*, vol. 136, no. 1, pp. 84–92, July 2004.
- [11] J. Krucker, A. Viswanathan, J. Borgert, N. Glossop, Y. Yanga, and B. J. Wood, "An electro-magnetically tracked laparoscopic ultrasound for multi-modality minimally invasive surgery," in *Comput. Assist. Radiol. Surg.*, Berlin, Germany, Jun. 2005, pp. 746–751.
- [12] M. Kleemann, P. Hildebrand, M. Birth, and H. P. Bruch, "Laparoscopic ultrasound navigation in liver surgery: Technical aspects and accuracy," *Surgical Endoscopy*, vol. 20, no. 5, pp. 726–729, May 2006.
- [13] J. Harms, H. Feussner, M. Baumgartner, A. Schneider, M. Donhauser, and G. Wessels, "Three-dimensional navigated laparoscopic ultrasonography," *Surgical Endoscopy*, vol. 15, pp. 1459–1462, 2001.
- [14] M. Nakamoto, Y. Sato, M. Miyamoto, Y. Nakamjima, K. Konishi, M. Shimada, M. Hashizume, and S. Tamura, "3-D ultrasound system using a magneto-optic hybrid tracker for augmented reality visualization in laparoscopic liver surgery," in *Proc. Int'l Conf. Medical Image Computing and Computer Assisted Intervention (MICCAI)*, T. Dohi and R. Kikinis, Eds. New York: Springer-Verlag, vol. 2489, Lecture Notes in Computer Science.
- [15] K. Konishi, M. Nakamoto, Y. Kakeji, K. Tanoue, H. Kawanaka, S. Yam-aguchi, S. Leiri, Y. Sato, Y. Maehara, S. Tamura, and M. Hashizume, "A real-time navigation system for laparoscopic surgery based on three-dimensional ultrasound using magneto-optic hybrid tracking configuration," *Int. J. Comput. Assist. Radiol. Surg.*, vol. 2, no. 1, pp. 1–10, Jun. 2007.
- [16] M. Nakamoto, K. Nakada, Y. Sato, K. Konishi, M. Hashizume, and S. Tamura, "Intraoperative magnetic tracker calibration using a magneto-optic hybrid tracker for 3-d ultrasound-based navigation in laparoscopic surgery," *IEEE Trans. Med. Imag.*, vol. 27, no. 2, pp. 255–270, Feb. 2008.
- [17] J. B. Hummel, M. R. Bax, M. L. Figl, Y. Kang, C. Maurer Jr., W. W. Birkfellner, H. Bergmann, and R. Shahidi, "Design and application of an assessment protocol for electromagnetic tracking systems," *Med. Phys.*, vol. 32, no. 7, pp. 2371–2379, Jul. 2005.
- [18] C. Nafis, V. Jensen, L. Beaugard, and P. Anderson, K. R. Cleary and R. L. Galloway Jr., Eds., "Method for estimating dynamic em tracking accuracy of surgical navigation tools," in *Med. Imag. 2006: Visualization, Image-Guided Procedures, Display*, Mar. 2006, vol. 6141, pp. 61410K-1–61410K-16.

- [19] V. V. Kindratenko, "A survey of electromagnetic position tracker calibration techniques," *Virtual Reality: Res. Develop., Appl.*, vol. 5, no. 3, pp. 169–182, 2000.
- [20] I. W. M. Wells, A. C. F. Colchester, and S. L. Delp, Eds., "Concepts and results in the development of a hybrid tracking system for CAS," in *Proceedings of the First International Conference of Medical Image Computing and Computer-Assisted Intervention (MICCAI)*. New York: Springer, vol. 1496, pp. 343–351.
- [21] D. Mucha, B. Kosmecki, and J. Bier, "Plausibility check for error compensation in electromagnetic navigation in endoscopic sinus surgery," *Int. J. Comput. Assist. Radiol. Surg.*, vol. 1, pp. 316–318, Jun. 2006.
- [22] T. Sielhorst, M. Feuerstein, and N. Navab, "Advanced medical displays: A literature review of augmented reality," *IEEE/OSA J. Display Technol.*, vol. 4, no. 4, pp. 451–457, Dec. 2008.
- [23] M. Feuerstein, T. Reichl, J. Vogel, A. Schneider, H. Feussner, and N. Navab, "Magneto-optic tracking of a flexible laparoscopic ultrasound transducer for laparoscope augmentation," in *Proc. Int'l Conf. Medical Image Computing and Computer Assisted Intervention (MICCAI)*. New York: Springer-Verlag, vol. 4791, Proc. Int'l Conf. Medical Image Computing and Computer Assisted Intervention (MICCAI), pp. 458–466.
- [24] M. Feuerstein, T. Reichl, J. Vogel, J. Traub, and N. Navab, "New approaches to online estimation of electromagnetic tracking errors for laparoscopic ultrasonography," *Comput. Assist. Surg.*, vol. 13, no. 5, pp. 311–323, Sep. 2008.
- [25] T. Sielhorst, M. Feuerstein, J. Traub, O. Kutter, and N. Navab, "Campar: A software framework guaranteeing quality for medical augmented reality," *Int. J. Comput. Assist. Radiol. Surg.*, vol. 1, pp. 29–30, Jun. 2006.
- [26] M. Feuerstein, T. Mussack, S. M. Heining, and N. Navab, "Intraoperative laparoscope augmentation for port placement and resection planning in minimally invasive liver resection," *IEEE Trans. Med. Imag.*, vol. 27, no. 3, pp. 355–369, Mar. 2008.
- [27] T. Yamaguchi, M. Nakamoto, Y. Sato, K. Konishi, M. Hashizume, N. Sugano, H. Yoshikawa, and S. Tamura, "Development of a camera model and calibration procedure for oblique-viewing endoscopes," *Comput. Aid. Surg.*, vol. 9, no. 5, pp. 203–214, 2004.
- [28] S. De Buck, F. Maes, A. D'Hoore, and P. Suetens, "Evaluation of a novel calibration technique for optically tracked oblique laparoscopes," in *Proc. Int'l Conf. Medical Image Computing and Computer Assisted Intervention (MICCAI)*. New York: Springer-Verlag, vol. 4791, Lecture Notes in Computer Science, pp. 467–474.
- [29] R. Prager, R. Rohling, A. Gee, and L. Berman, "Rapid calibration for 3-d freehand ultrasound," *Ultrasound Med. Biol.*, vol. 24, no. 6, pp. 855–869, 1998.
- [30] G. M. Treece, A. H. Gee, R. W. Prager, C. J. C. Cash, and L. H. Berman, "High-definition freehand 3-d ultrasound," *Ultrasound Med. Biol.*, vol. 29, no. 4, pp. 529–546, 2003.
- [31] P.-W. Hsu, R. W. Prager, A. H. Gee, and G. M. Treece, "Rapid, easy and reliable calibration for freehand 3-D ultrasound," *Ultrasound Med. Biol.*, vol. 32, no. 6, pp. 823–835, Jun. 2006.
- [32] T. Langø, "Ultrasound guided surgery: Image processing and navigation," Ph.D. dissertation, Norwegian Univ. Sci. Technol., Trondheim, Oct. 2000.
- [33] Y. Baillot, S. Julier, D. Brown, and M. Livingston, "A tracker alignment framework for augmented reality," in *Proc. IEEE ACM Int. Symp. Mixed Augmented Reality (ISMAR)*, Oct. 2003, pp. 142–150.
- [34] W. Birkfellner, F. Watzinger, F. Wanschitz, R. Ewers, and H. Bergmann, "Calibration of tracking systems in a surgical environment," *IEEE Trans. Med. Imag.*, vol. 17, no. 5, pp. 737–742, Oct. 1998.
- [35] R. Tsai and R. Lenz, "Real time versatile robotics hand/eye calibration using 3-D machine vision," in *Proc. IEEE Int. Conf. Robot. Automat.*, 1988, vol. 1, pp. 554–561.
- [36] Y. Shiu and S. Ahmad, "Calibration of wrist-mounted robotic sensors by solving homogeneous transform equations of the form $ax = xb$," *IEEE Trans. Robot. Autom.*, vol. 5, no. 1, pp. 16–29, Feb. 1989.
- [37] K. Daniilidis, "Hand-eye calibration using dual quaternions," *Int. J. Robot. Res.*, vol. 18, pp. 286–298, 1999.
- [38] T. Reichl, "Online error correction for the tracking of laparoscopic ultrasound," M.S. thesis, Technische Universität München, Jul. 2007.
- [39] P. E. Gill, W. Murray, and M. H. Wright, "The Levenberg-Marquardt method," in *Practical Optimization*. New York: Academic, 1981, pp. 136–137, ch. 4.7.3.
- [40] K. Nakada, M. Nakamoto, Y. Sato, K. Konishi, M. Hashizume, and S. Tamura, "A rapid method for magnetic tracker calibration using a magneto-optic hybrid tracker," in *Proc. Int'l Conf. Medical Image Computing and Computer Assisted Intervention (MICCAI)*, T. M. Peters, Ed. New York: Springer, 2003, vol. 2879, Lecture Notes in Computer Science, pp. 285–293.
- [41] X. Wu and R. Taylor, "A direction space interpolation technique for calibration of electromagnetic surgical navigation systems," in *Proc. Int'l Conf. Medical Image Computing and Computer Assisted Intervention (MICCAI)*, R. E. Ellis and T. M. Peters, Eds. New York: Springer-Verlag, 2003, vol. 2879, Lecture Notes in Computer Science, pp. 215–222.
- [42] W. J. Youden, "Index for rating diagnostic tests," *Cancer*, vol. 3, no. 1, pp. 32–35, 1950.
- [43] G. Welch and G. Bishop, "Course 8—an introduction to the kalman filter," SIGGRAPH 2001 [Online]. Available: http://www.cs.unc.edu/~tracker/media/pdf/SIGGRAPH2001_CoursePack_08.pdf
- [44] A. Doucet, N. De Freitas, and N. Gordon, Eds., *Sequential Monte Carlo Methods in Practice*. New York: Springer, 2001.